Winter 2014

Ionizing Radiation Detection Using Microstructured Optical Fiber

Stanton DeHaven
Old Dominion University

IONIZING RADIATION DETECTION USING

MICROSTRUCTURED OPTICAL FIBER

by

Stanton DeHaven
B.S.M.E. May 1984, University of Kentucky
M.S.M.E. May 1987, University of Kentucky
M.E.E.E. December 2001, Old Dominion University

A Dissertation Submitted to the Faculty of
Old Dominion University in Partial Fulfillment of the
Requirements for the Degree of

DOCTOR OF PHILOSOPHY

ELECTRICAL ENGINEERING

OLD DOMINION UNIVERSITY
December 2014

Approved by:

_____
Sacharia Albin (Director)

_____
Mounir Laroussi (Member)

_____
Frederic McKenzie (Member)

_____
William Winfree (Member)

ABSTRACT

IONIZING RADIATION DETECTION USING MICROSTRUCTURED OPTICAL FIBER

Stanton DeHaven
Old Dominion University, 2014
Director: Dr. Sacharia Albin

Ionizing radiation detecting microstructured optical fibers are fabricated, modeled and experimentally measured for X-ray detection in the 10-40 keV energy range. These fibers operate by containing a scintillator material which emits visible light when exposed to ionizing radiation. An X-ray source characterized with a CdTe spectrometer is used to quantify the X-ray detection efficiency of the fibers. The solid state CdTe detector is considered 100% efficient in this energy range. A liquid filled microstructured optical fiber (MOF) is presented where numerical analysis and experimental observation leads to a geometric theory of photon transmission using total internal reflection. The model relates the quantity and energy of absorbed X-rays to transmitted and measured visible light photons. Experimental measurement of MOF photon counts show good quantitative agreement with calculated theoretical values. This work is extended to a solid organic scintillator, anthracene, which shows improved light output due to its material properties. A detailed description of the experimental approach used to fabricate anthracene MOF is presented. The fabrication technique uses a modified Bridgman-Stockbarger crystal growth technique to grow anthracene single crystals inside MOF. The anthracene grown in the MOF is characterized using spectrophotometry, Raman spectroscopy, and X-ray diffraction. These results show the anthracene grown is a high purity crystal with a structure similar to anthracene grown from the liquid, vapor and melt techniques. The X-

ray measurement technique uses the same approach as that for liquid filled MOF for efficiency comparison. A specific fiber configuration associated with the crystal growth allows an order of magnitude improvement in X-ray detection efficiency. The effect of thin film external coatings on the measured efficiency is presented and related to the fiber optics. Lastly, inorganic alkali halide scintillator materials of CsI(Tl), CsI(Na), and NaI(Tl) are grown as single crystals inside the MOF. These alkali halide fibers show an improvement in X-ray detection efficiency comparable with the CdTe detector and can be more efficient, dependent upon the photon counter efficiency and fiber configuration. The fiber configuration for this improved efficiency is described as the same for the higher efficiency anthracene MOF.

ACKNOWLEDGMENTS

I would like to thank my advisor, Dr. Albin for his guidance, efforts, and patience towards this goal. His knowledge, inspiration, and persistence have been invaluable in this work. I would also like to express my gratitude to Dr. Mounir Laroussi, Dr. Frederic McKenzie and Dr. William Winfree for being part of my dissertation committee and taking time from their schedules for me to complete this dissertation. The nondestructive evaluation sciences branch (NESB) at NASA Langley deserves special recognition for their support and encouragement through this work. Many persons at NASA Langley helped to complete this work including Patty Davis, Dr. Phillip Williams, Dr. Russell (Buzz) Wincheski, and Dr. William (Cy) Wilson. The encouragement and guidance by Dr. William Winfree as my former Branch head helped build the foundation for this effort and the encouragement by Elliot Cramer as my current Branch head has allowed this work to continue. Also, I would like to express my gratitude to the late Warren Kelliher whose X-ray fluorescence equipment was used in this work along with the late Dr. Robert Rogowski who inspired confidence and provided encouragement. Lastly, I would like to thank Dr. Mounir Laroussi, Dr. Hani Elsayed-ali, and Dr. Michael Kelley for their courses in plasmas and material characterization which presented the many practical uses for ionizing radiation and captured my imagination.

TABLE OF CONTENTS

LIST OF TABLES

Table   Page

LIST OF FIGURES

CHAPTER I

INTRODUCTION

OVERVIEW OF WORK

This dissertation presents ionizing radiation detection using microstructured optical fiber. Ionizing radiation is a type of electromagnetic radiation associated with higher energies and shorter wavelengths. The ability of particles or higher energy electromagnetic waves to dislodge an outer shell electron creates an ion and gives this electromagnetic energy its name [1].

Some common types of ionizing radiation are X-rays, electron beams, α-particles, β-particles, γ-rays, neutrons (indirect), and ultraviolet light. Common sources of ionizing radiation are X-ray tubes, isotopes, electron guns, cosmic rays, nuclear reactors, and sunlight. Typical uses for ionizing radiation are: nondestructive examination (NDE) such as X-ray weld examination, Computed Tomography, dental X-rays; food sterilization; smoke detectors; static electricity eliminators; medical cancer treatments and radioactive tracers for medical diagnosis; chemical analysis using X-ray fluorescence; electron microscopes; X-ray diffraction scans and crystallography; and as a pump for lasers. Some more recent uses of X-ray detection are atmospheric lightning discharge and X-ray microscopy.

The detection of ionizing radiation with microstructured optical fiber is performed by incorporating a scintillator material in the optical fiber. Scintillators detect all the

common forms of ionizing radiation including electrons, α-particles, β-particles, γ-particles, neutrons, X-rays and gamma rays [2]. Although the precise ionization energy level varies with individual atoms and molecules, a general statement is that any radiation with a quantum energy above 10 electron volts is ionizing radiation based on the 13.6 electron volt ionization energy of hydrogen [1].

In this work, X-rays were the chosen form of ionizing radiation. X-rays have several advantages for ionizing radiation detector research. These are: the ease of producing X-rays using an X-ray tube along with the control of energy and quantity; the relative ease of containing and stopping X-rays; the availability of X-ray spectrometers to characterize the X-rays; detectors which are near 100% efficient over a range of X-ray energies; and only slight attenuation from air at close range. The attributes of X-rays allow a quantifiable approach to determine the efficiency of new detectors.

There are multiple techniques to detect ionizing radiation. The Geiger-Muller counter is possibly the most well-known and relies on ionizing radiation passing through low pressure gas in a tube to create electrical conductivity. This electrical conductivity creates a pulse of current which is multiplied by the Townsend avalanche effect and associated electronics so a pulse of current can be associated with each ionizing event. More modern detectors use semiconductors to create electron-hole pairs from the ionizing radiation absorption. Scintillators are materials which convert absorbed ionizing radiation into visible light [2].

Microstructured optical fiber detects ionizing radiation by guiding light emitted by scintillating materials in the fiber. In this work, both a liquid and solid are used. Liquid is

introduced in the fiber using capillary action and solid scintillators are grown in the fiber by a crystal growth from the melt. X-rays can be detected with both liquid and solid filled microstructured optical fiber.

The microstructured fiber is also known as photonic crystal fiber (PCF) or holey fiber. These names come from the holes in the quartz which are configured in a specific geometric pattern. Two primary types of this fiber are band-gap and effective index fibers, named for their light transmission properties. The bandgap fibers often have a hollow core and light is transmitted due to the geometric pattern symmetry while the effective index fibers transmit light through a core surrounded by a geometric pattern cladding. This pattern is based on symmetry considerations associated with crystal structure and band structures analogous to Brillion zones [3].

Microstructured optical fiber has been applied towards sensing by filling with liquids, placing chemical coatings inside, at the end, and on the outside of optical fiber, using quantum dots, and carbon nanoparticles. These filled microstructured fiber sensors operate on various principles including fluorescence, absorption, and refractive index changes [4-9]. Liquid filled fibers have been considered for many sensing and detection applications [10-14]. The various liquids and coating offer broad range of unique sensing and detection capabilities.

The solid core microstructured optical fiber operates similar to typical index guided mode fiber where the core has a higher index of refraction than the cladding over a wide range of wavelengths. However, there are specific wavelengths where the microstructured cladding acts to transmit a range of wavelengths using band-gap effects.

The hollow core photonic crystal fiber operates entirely on band-gap effects with the microstructure geometry allowing light transmission [15-16].

Upon initial fabrication, air fills the pores or holes in the fiber microstructure. The microstructured cladding and band-gap transmission is primarily evanescent modes which have a complex effective index of refraction compared to guided modes which have a real index of refraction. This leads to band-gap and evanescent light transmission being more 'leaky' and less efficient, but also more interaction of the light with the cladding which can be useful for sensing [17].

When used as sensing fiber, either a coating on the walls of the microstructured geometry or liquid or solid material fill these holes and become part of the geometry. Dependent on the index of refraction properties of the filling material, guided or band-gap transmission occurs. Gases other than air or quantum dots and carbon nanoparticles on the walls only change the transmission properties slightly [5-6]. The theoretical work presented here uses liquids and solid to fill the microstructured optical fiber which results in guided modes with a real index of refraction for light transmission.

The materials selected for filling the microstructured fiber were chosen based on their scintillation properties. Both organic and inorganic scintillators are available but organics were initially chosen because they exist in liquids and the solid form is relatively easy to obtain [18]. Inorganic scintillators are typically alkali halide salts of the NaI and CsI type doped with thallium or sodium. The organic solid scintillator used is the pure compound, anthracene, which can be obtained in scintillation grade. The alkali halide scintillators are well-known and extensively used for gamma and X-ray detection [19].

The standard scintillation fiber is plastic, PMMA, with an organic scintillator doped core [20]. Because of the plastic optical properties, the core must be fairly large ~ 1mm in diameter and the cladding is relatively thin. Attenuation is fairly high in these plastic fibers and they will darken from X-ray absorption over time but they have been used for neutron and particle physics experiments. For higher energy X-rays, suitable for NDE use, glass core scintillation fibers are more suitable [21]. Both the glass core and plastic scintillator fibers guide light on the principle of total internal reflection. The plastic and glass fibers are coupled to a photo detector for light pulse measurements.

The microstructured optical fiber (MOF) presented contains a scintillating material which emits visible light upon absorption of X-rays. This light is transmitted by the optical fiber to a photo detector. The quartz microstructured geometry can behave as a cladding, similar to PMMA or glass core scintillation fiber. However, this dissertation presents another mechanism of light transmission that can occur which allows significantly more light transmitted by a solid scintillator material in the microstructured optical fiber. Two light guiding mechanisms have been found in this work with microstructured optical fiber: one from total internal reflection (TIR) and a second which is more complex that includes TIR effects but also microstructured optics which capture and direct more of the scattered scintillator light to a photo detector.

SCOPE OF RESEARCH.

This work incorporates the theoretical modeling, fabrication, characterization, experimental testing and verification of microstructured optical fiber as an ionizing radiation detector using X-rays. Theory is presented for scintillation light generation and

transmission in the optical fiber along with a qualitative theoretical approach to crystal growth inside microstructured optical fiber. An experimental approach to measuring the X-ray detection output is described with the results compared to fiber TIR theoretical maximum output calculations [22]. The experimental technique to grow continuous anthracene crystals inside microstructured fiber is described. Characterization results of the anthracene fibers grown in the microstructured optical fiber using fluorescence spectrophotometry, X-ray diffraction, and Raman spectroscopy are presented [23]. This same experimental technique to grow anthracene crystals is applied to alkali halide crystal growth inside microstructured optical fiber [24]. The output of liquid, anthracene, and alkali halide optical fibers is compared to a CdTe semiconductor detector over an energy range from 10 to 40 keV where the CdTe detector is considered 100% efficient.

The chronological sequence of this work began with modeling the waveguide characteristics of liquid filled MOF and solid anthracene filled MOF [25]. A technique for filling the fiber with liquid was established along with preliminary work for growing anthracene as a single crystal inside MOF. An experimental setup was configured using laboratory X-ray fluorescence equipment with the X-ray spectrometer to characterize the X-ray tube using a CdTe type detector for ease of X-ray photon counting. The X-ray spectrometer was arranged using a collimator oriented to represent a fiber, then replaced with a fiber and the X-ray scintillation recorded using a photon-counting technique. With the liquid-filled and preliminary anthracene fiber compared to the theoretical model, the focus changed to improving the crystal growth of the anthracene fiber to improve the efficiency. Improvement in fiber output was shown after incorporating the qualitative thermodynamics theory and modifications to the experimental parameters. Microscope

images were used as the initial inspection technique to assess the growth parameter changes. Subsequent characterization using fluorescence spectrophotometry, Raman spectroscopy, and X-ray diffraction was performed to evaluate the quality of the anthracene crystal grown in the MOF. Alkali halide scintillator materials were introduced using the configuration developed for anthracene with the temperatures adjusted to the higher melting points.

The analysis and modeling used two software packages, FIMMWAVE and CUDOS to determine the operating transmission modes of the fiber when used as an X-ray detector [26-27]. Once the transmission modes were determined, a fiber optic model was constructed incorporating the effects of X-ray interactions and the resultant light guidance based on total internal reflection (TIR) theory. The model was derived from the analysis and fundamental waveguide theory using TIR. This TIR model was then used to establish a maximum theoretical output from the fiber for comparison with experimental data.

The anthracene fiber crystal growth comprised a significant portion of this work. Initially, it was considered that a patented technique for organic crystal growth in optical fiber would be used to grow the anthracene crystals. However, it was recognized that the patented technique did not work for the anthracene fiber which lead to considering thermodynamic theory and expanded crystal growth experiments. Development of anthracene fiber crystal growth aided the eventual growth of alkali halide fiber.

Growing alkali halide crystals inside MOF using the same experimental apparatus for anthracene was found to be successful. The CsI(Tl) fiber was grown initially and

experimental observations indicated that significant light is emitted from the fiber with a portion having an air gap [24]. This air gap forms due to the higher density of the solid when compared to the liquid for anthracene or alkali halide fibers. The alkali halide MOF with this air gap was found experimentally to be significantly more efficient than fiber containing only scintillator material. The alkali halide materials NaI(Tl) and CsI(Na) demonstrated similar higher efficiencies with a fiber air gap to CsI(Tl). Based on these observations, the anthracene fiber was grown again with an air gap and also demonstrated significantly higher efficiencies compared to previous work.

In an attempt to understand more of the optical effect from the air gap, two thin film coatings were applied on the anthracene fiber. These were aluminum and polytetrafluoroethylene (PTFE). A similar approach was taken with the alkali halide fibers using only an aluminum thin film. In all cases, these sputter coated films decreased the X-ray detection efficiency when applied to the fiber exterior. The coatings were applied to fibers that were previously measured for efficiency.

The theory in Chapter II describes the scintillator material behavior and properties, conversion of photons to electrons for measurement, fiber waveguide analysis and modeling, maximum photon output from X-ray interaction, and crystal growth from the melt thermodynamics. The experimental portion in Chapter III describes the X-ray measurements and fiber configuration to characterize the X-ray tube energy and photon output, photomultiplier configuration for the X-ray detecting fiber, liquid filled fiber preparation, anthracene crystal growth experimental work, preparation of the anthracene fiber for analytical characterization and alkali halide crystal growth. The results in Chapter IV are presented and discussed for the TIR theoretical analysis and model,

comparison of the fiber X-ray detection compared to theory and relative efficiency, growth of the anthracene fiber and processing considerations, anthracene crystal characterization, and alkali halide growth and processing considerations. This work is summarized and future work considerations are presented in Chapter V.

CHAPTER II

THEORY

SCINTILLATOR PROPERTIES

Scintillation is the emission of light in a wavelength longer than the absorbed light and is theoretically the same as fluorescence. The term scintillation in the context of this work describes visible light emission from absorbing an X-ray photon. This same visible light can occur when absorbing an ultraviolet (UV) photon, but is instead termed fluorescence. In both cases, the absorption of a shorter, higher energy wavelength causes a re-emission of a longer, lower energy, wavelength [18].

The molecular structure of the liquid and anthracene materials allows the fluorescent and ionizing radiation scintillation phenomenon to occur. The BC-517H scintillation liquid and anthracene solid organic materials both have a similar molecular structure. This similar structure is linked to a benzene hydrocarbon ring and π orbital electrons [2, 18]. Fig. 1 shows a diagram of the orbital structure with related fluorescence and phosphorescence. The alkali halide materials have ionic bonds described in inorganic chemistry and form a crystal lattice. The absorption of an X-ray and subsequent emission of light is more closely linked to the crystal lattice structure and shared electrons with a trace activator (dopant) material. The NaI(Tl) and CsI(Tl) materials have thallium (Tl) as the activation element with CsI(Na) having sodium (Na) [19]. Fig. 2 shows a diagram of the energy band structure of these alkali halide scintillators. This dissertation uses the organic scintillators BC-517H liquid, solid crystalline anthracene, and the alkali halides NaI(Tl), CsI(Tl), and CsI(Na).

Theory: π orbital energies
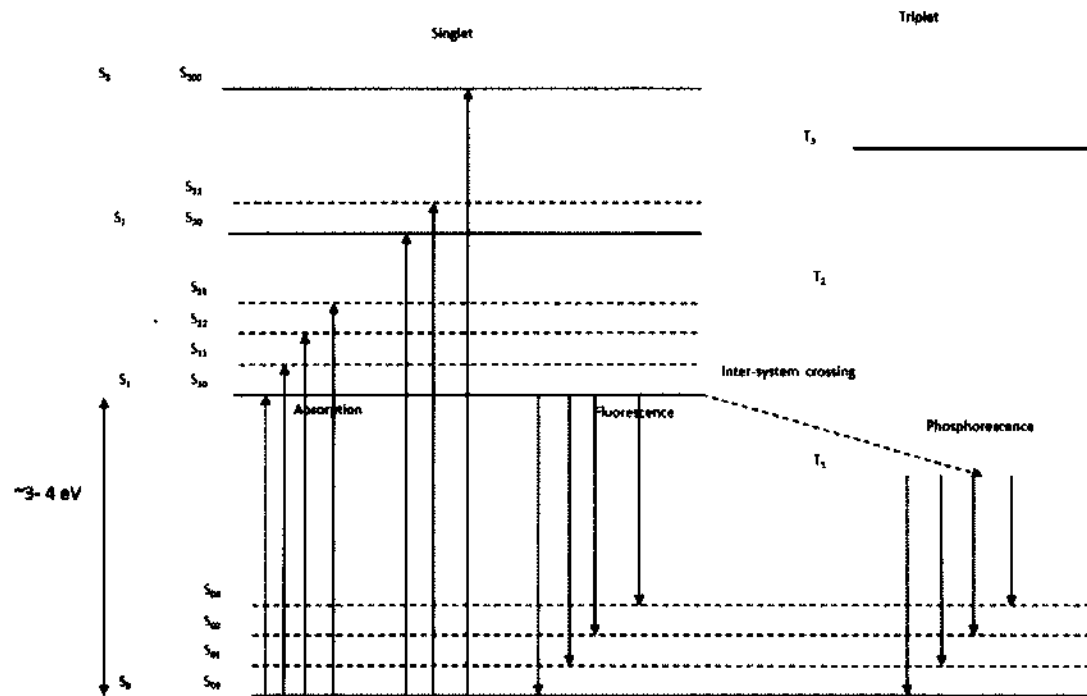
Figure 1. Organic scintillator pi-orbital energy absorption re-emission energy diagram
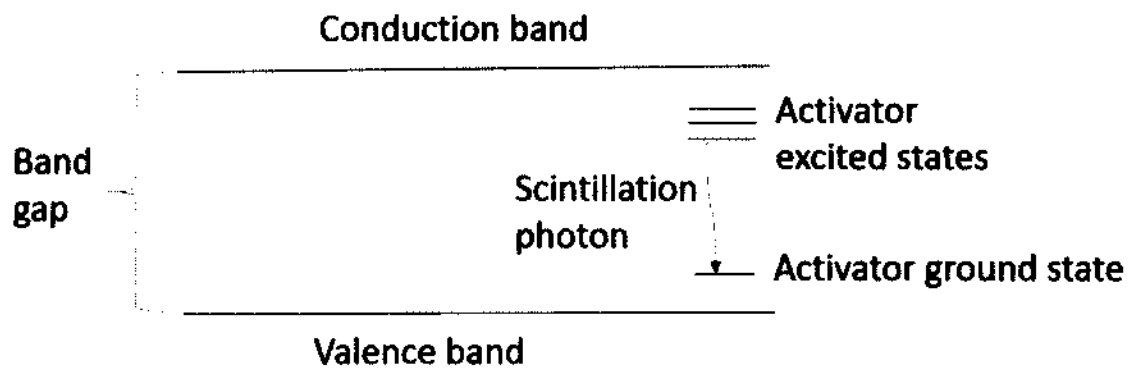
Figure 2. Alkali halide activated (doped) crystalline scintillator energy band structure.

The photon absorption and re-emission are energy conserving events. The emitted photon is always at a lower energy, or longer wavelength, than the absorbed photon with the energy relation given by Planks law [1]:

$$E = h\nu \tag{1}$$

where h is planks constant and ν is the photon frequency. This photoelectric effect occurs when energy E exceeds the work function E_o and

$$E_o = h\nu_o \tag{2}$$

where ν_o is a threshold frequency for the electron. For a given energy E greater than E_o the electron absorbs the difference $E-E_o$ resulting in the emitted photon frequency

$$\nu = (E - E_o)/h \tag{3}$$

with the resultant wavelength, λ, given by:

$$\lambda = c/\nu \tag{4}$$

where c is the speed of light in vacuum. This photoelectric effect is common to all scintillators [18, 19].

Both inorganic and organic scintillators are used for ionizing radiation with higher energy photons associated with inorganic and lower energies and neutron detection associated with organic compounds. The light output from inorganic scintillators, while greater than those of the organics, is only 2-3 times larger. However, the primary reason for using inorganic scintillators for high energy 'hard' X-rays and gamma rays comes

from the higher density and molecular weight to stop and absorb the higher energy X-ray

photons. Table 1. shows the relative light output of various current fiber scintillators [2].

Table 1. Typical light yield for fiber scintillators.

Core Material	Photons/keV	λ_{peak}(nm)
Glass Scintillator	3-5	400
Plastic Scintillator	8-10	420
Liquid Scintillator	7-13	420

For gamma ray detection NaI(Tl) is the predominant inorganic scintillation crystal

and CsI(Tl) is also a frequently used scintillator [19]. Compared to fiber scintillators,

inorganics have ~ 2-4x more output and use atomic, rather than molecular, photoelectric

effects. However, the basic phenomenon also uses equations (1) through (4). Table 2

shows the relative light output of scintillators used in this work [2,18,19].

Table 2. Typical light yield, emission wavelength, fluorescence, and index of refraction for inorganic and organic scintillators.

Scintillator	Photons/keV	Emission wavelength λ_{peak}(nm)	Fluorescence under UV excitation?	Fluorescence excitation wavelength (nm)	Index of refraction (n_{eff})
Sodium Iodide (w/Thallium), Inorganic	36	415-420	Y	254	1.82
Cesium Iodide (w/Thallium), Inorganic	62	550	Y	254	1.79

Cesium Iodide (w/Sodium), Inorganic	38	420	N	NA	1.79
Liquid Scintillator (BC-517H), Organic	7.5	425	Y	385	1.476
Anthracene crystal, Organic	16	425	Y	385	1.62

The gamma or X-ray monochromatic energy encountering a scintillator will impart a fraction of the energy, E_i, related by [2]:

$$E = (1 - e^{-\alpha d})E_i \tag{5}$$

where E_i is the incident photon energy, d is the thickness, and α is the overall absorption expressed as:

$$\alpha = \alpha_{ab} + \alpha_c + \alpha_{pp} \tag{6}$$

where α_{ab} is photo-electric absorption, α_c is Compton scattering, and α_{pp} is pair production.

The increased density and higher molecular weight of the inorganic scintillators, such as NaI(Tl) and CsI(Tl) results in more Compton scattering per unit length. Pair production occurs for energy ranges above 1.02 MeV. For lower energy levels, photo-electric absorption is the predominant mechanism.

In Compton scattering the electrons produced by incident photons of energy E_i are related by:

$$E_c = E_i/(1 + m_o c^2/2E_i) \tag{7}$$

where $m_o c^2$ is the electron rest energy of 0.51 MeV. The pair production residual energy E_{PP} is:

$$E_{pp} = E_i - 2m_o c^2 \tag{8}$$

The X-ray energies used in this work ranged in energy from 10 keV to 40 keV. As such, Compton and pair production energies were not considered significant for the scintillator materials and only photo-electric absorption was considered [2].

CONVERSION OF PHOTONS TO ELECTRONS

The conversion of photons to electrons is necessary to measure scintillation output. The photon absorption generates an electron due to the photoelectric effect. Traditional scintillation devices used photomultiplier tubes for photon to electron conversion. These tubes have a cathode which emits electrons from absorbed photons and an internal configuration which amplifies the number of electrons generated at the tube anode. The solid state photomultiplier devices use semiconductor material to generate electrical current from photon absorption. The solid state devices can operate at higher quantum efficiencies compared to photomultiplier tubes but have higher dark current noise.

Photomultiplier tube theory: photocathode emitted electrons; dynode amplification of electrons; current output related to number of photons; noise is primarily electronic. Fig. 1 shows a scintillator coupled to a photomultiplier tube.

Photocathode Electrons Anode

Incident photon Electrical connectors

Scintillator

Light photon Focusing electrode Dynode

Photomultiplier tube (PMT)
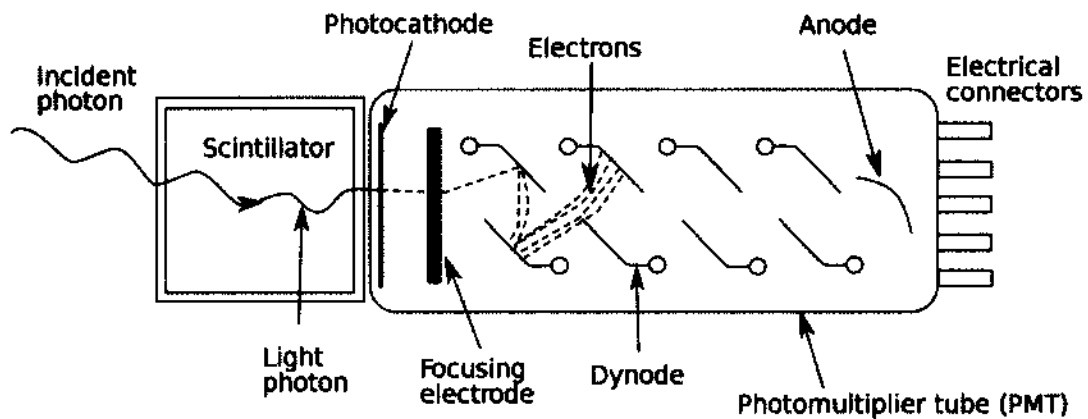
Figure 3. Photomultiplier tube showing cathode, dynodes, and anode with direction of amplified electrons from cathode to anode.

Solid state photo detector theory: photons interact directly with the semiconductor surface and form electron-hole pairs; current from photodiode is directly related to the electron-hole production; quantum efficiency is higher because of this effect but so is dark noise from temperature effects; cooling reduces dark noise.

A photon counting module, used with CsI(Tl) scintillating fiber, uses a silicon photon avalanche semiconductor detector which has peak efficiency at 700 nm. The detector active surface diameter is 180 microns and the semiconductor is thermoelectrically cooled and temperature controlled. The cooling reduces dark noise and temperature control determines the noise bounds. The efficiency of the avalanche photodiode is over 70% at 700 nm and ~ 60% at 550 nm for the Pacer SPCM-AQRH-15-FC module used.

Additionally, the photon counting module as a dark count rating of 50/s with a high TTL signal level of 2.2 V with a maximum dead time of 20 ns. A single output with a 50 ohm impedance provides the conditioned TTL voltage. A one volt trigger level is

recommended when collecting data from these electronics to avoid triggering on noise.

The photon counting module is a solid state device containing the conditioning

electronics with no adjustments for photon detection sensitivity. A diagram of a typical

avalanche photo diode is shown in Fig. 4.

Silicon Avalanche photo diode diagram
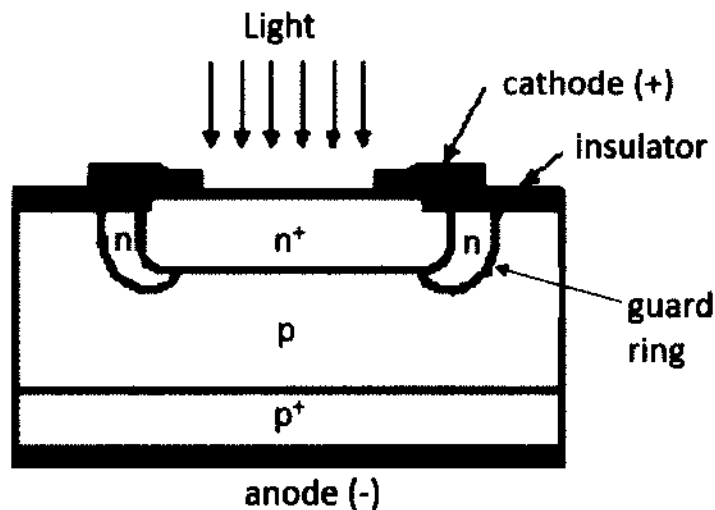
Figure 4. Diagram of an avalanche silicon photodiode where a single photon causes a cascade of electrons from the anode to the cathode.

WAVEGUIDE PROPERTIES

The use of microstructured optical fiber for sensing allows operation as a waveguide

in several modes. Some of the modes have imaginary mathematical components in the

index of refraction associated with band-gap effects, others are related to evanescent

wave transmission and the effective index of refraction between the cladding and core,

and some are associated with guided modes where the index of refraction is real with no

imaginary components. Depending on the wavelength, and components in the cladding, a microstructured optical fiber transmits in one or more of these modes.

For the microstructured fiber filled with optically transparent liquid or solid material, the filling material has an index of refraction higher than quartz so the combined quartz and filled region index of refraction will be higher than a core. The total internal reflection approach to guiding light requires the cladding to have a lower index of refraction than the core. When this does not occur, band gap transmission of light is still possible. However, the wavelengths allowed for transmission may not be useful. Additionally, band-gap light transmission is inherently less efficient than guided mode transmission due to the evanescent effects from the effective imaginary refractive index of the material. However, this same evanescent effect can provide the operating mechanism for a fiber optic sensor.

The liquid filled microstructured optical fiber used in this work was analyzed using the CUDOS and FIMMWAVE software packages. The CUDOS package uses a multi-pole method for solving the modes of light transmission in an optical fiber with geometric variation in the index of refraction. FIMMWAVE is a software package which uses a finite element technique for solving the same light transmission modes. The material index of refraction must be provided with the wavelength of interest, as input parameters. The resulting solutions for the transmission modes provide the type of transmission. Real index of refractions in the solution are for guided modes and complex index of refractions are for evanescent or band-gap modes.

The solutions of these modes are wavelength dependent for a fixed geometry and materials. A unique solution can be found for a given geometry and materials for different wavelengths. In the case of the filled microstructured optical fibers, all the modal solutions showed the index of refraction was real with no complex components. The geometries for the CUDOS and FIMMWAVE software are shown in Figs. 5 and 6 respectively. The liquid optical fiber is modeled with both the CUDOS and FIMMWAVE software packages.
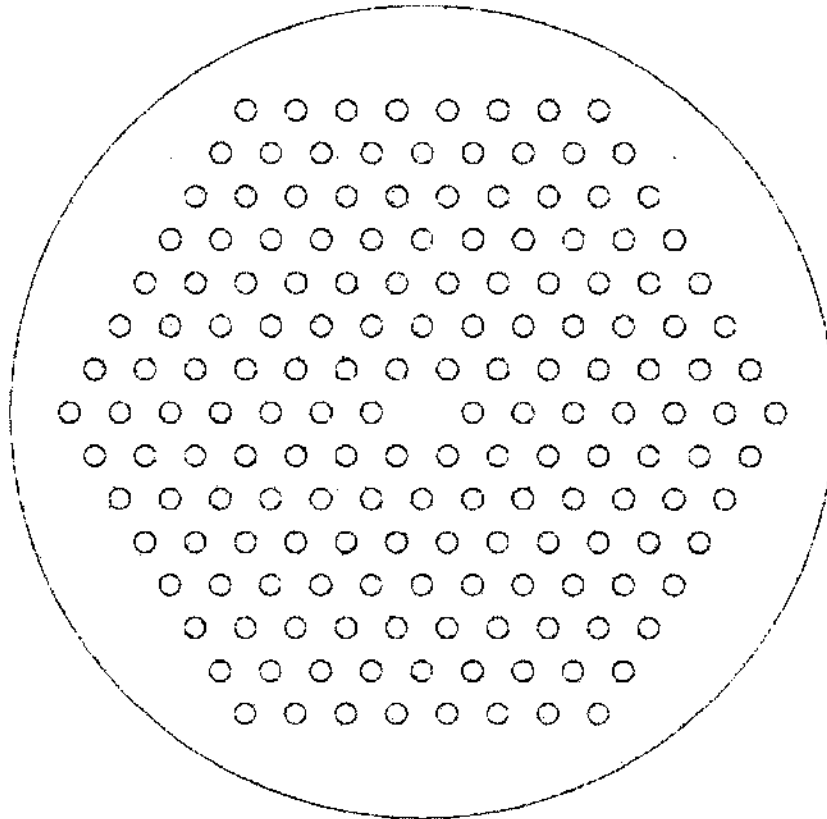
Figure 5. Fiber geometry used in FIMMWAVE for BC-517H liquid filled analysis.
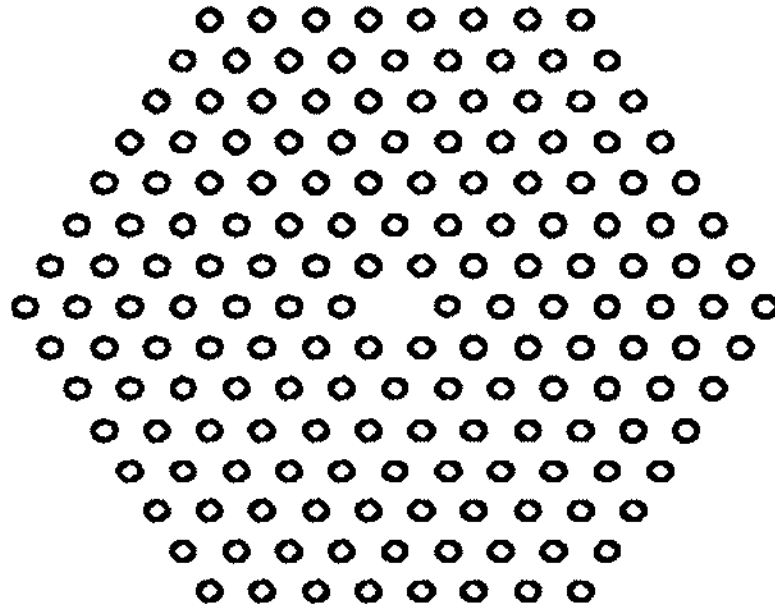
Figure 6. Fiber geometry used in CUDOS software for BC-517H liquid filled analysis.

The anthracene filled microstructured fiber solution was found using the

FIMMWAVE software package. The higher index of refraction of the anthracene

compared to the BC-517H liquid was a problem with the CUDOS software, which was

written for air filled photonic crystal fiber analysis and tailored for solution have a

complex index of refraction. The CUDOS software would not converge with the higher

index material of anthracene.

THEORETICAL MAXIMUM PHOTON OUTPUT OF FIBER FROM X-RAY INTERACTION

Based on the CUDOS analysis for the liquid and FIMMWAVE analysis for both the

liquid and anthracene filled microstructured optical fiber, all the modes calculated for

light transmission have a real index of refraction which is good for guided modes.

Hence, the model of the waveguide uses total internal reflection for real guided modes.

The guided modes total internal reflection model for liquid filled and anthracene fiber used weakly guiding theory.

The weakly guiding waveguide approximation is valid if $\Delta \ll 1$ as given by [28-29]:

$$\Delta = (n_i^2 - n_m^2)/2n_i^2 \qquad (9)$$

where n_i is the index of refraction of the liquid or anthracene in the inclusion and n_m is the index of refraction of the quartz cladding. For the BC-517H liquid, n_i=1.476, with n_m=1.458 for quartz cladding, and the anthracene index of refraction is 1.62. This yields $\Delta \approx 1\%$ for BC517H and $\Delta \approx 9\%$ for anthracene which indicates both materials are valid for the weakly guiding approximation.

The weakly guiding approximation allows total internal reflection theory. The liquid or anthracene inclusions are modeled as a bundle of weakly guiding multimode fibers with negligible mode coupling. Considering the liquid MOF as a multi-core fiber, evaluation of the normalized V parameter:

$$V = (2\pi\rho/\lambda)[n_i^2 - n_m^2]^{1/2} \qquad (10)$$

where ρ is the inclusion diameter and λ is the wavelength of the guided light. For a 425 nm wavelength with ρ=2500 nm, equation (10) yields V=8.375 for the BC-517H liquid and V=26.09 for anthracene and each filled inclusion is approximated as a step index multimode fiber. This allows analytical solutions from step index weakly guiding optical fiber theory. The number of modes is given by

$$N_m \approx V^2/2 \qquad (11)$$

Considering the photons from the scintillation process as rays from a spherical dipole, the complementary angle θ_c for guiding the photons is defined using:

$$\Delta = (^1/_2)sin^2\theta_c \tag{12}$$

where the complementary angle, θ_c, limits the angle of bound rays propagation in the fiber. The photon capture probability [30]:

$$P_{nc} = \int_0^{\theta_c} sin(\phi)d\phi \Big/ 2 = (1 - cos(\theta_c)) / 2 \tag{13}$$

is the ratio of surface area emitting thorough θ_c to the total spherical surface area. Using equations 9 and 12 with 13 yields $P_{nc} = 0.59\%$ for liquid BC-517H and $P_{nc} = 4.9\%$ for anthracene. For multimode power transmission the percent of power guided through bound modes is:

$$\eta_{wg} = P_{core}\Big/P \approx 1 - 4\Big/3\sqrt{N_m} \tag{14}$$

where P_{core} is the guided core power and P is the total power. Equations 10, 11, and 14 combine for a waveguide efficiency, $\eta_{wg} = 77\%$ for liquid BC-517H and $\eta_{wg} = 89\%$ for anthracene. The BC-517 liquid has an output of 7.5/keV with anthracene having an output of 16/keV photon emission. The number of emitted light photons per absorbed X-ray photon yields:

$$N_p(E) = \varepsilon E N(E) \tag{15}$$

where $\varepsilon = 7.5$ photons/keV for liquid BC-517H and $\varepsilon = 16$ photons/keV for anthracene,

E is the energy per X-ray photon in keV and $N(E)$ is the number of absorbed

monochromatic photons per unit time at energy E. Beer's law is:

$$I = I_o e^{-\alpha l} \tag{16}$$

and relates the absorbed X-ray photon intensity to length l using an absorption coefficient

α with

$$I = \frac{(h\nu)N}{A} \tag{17}$$

where A is the cross sectional area of the liquid or anthracene in the fiber. The intensity,

I, of the emerging photons from the material with initial intensity, I_o, uses Eq. (17). The

intensity of photons lost or absorbed in the material is given by:

$$I = I_o(1 - e^{-\alpha l}) \tag{18}$$

Combining Eq. (1), (18), and (19) allows writing:

$$N(E) = A_r(1 - e^{-\alpha l})N_{xrays}(E) \tag{19}$$

where $N_{xrays}(E)$ is the total number of X-ray photons at energy E with absorption

coefficient $\alpha(E)$ absorbed in the fiber liquid or anthracene of length l. A_r is the area ratio

between the 100 micron diameter collimator and 168 holes of 2.5 micron diameter:

$$A_r = \frac{168 \cdot 2.5^2}{100^2} = 0.105 \tag{20}$$

For both the liquid and anthracene, the absorption coefficient is approximated using

vinyl toluene data due to the similar hydrocarbon structure and absorption properties of

both scintillators. The photomultiplier quantum, collection, and transmission efficiencies

combine to an approximate detector efficiency $\eta_d = 18\%$. The maximum photomultiplier

electrical pulse count rate during X-ray exposure is:

$$N_c = \int N_p \, P_{nc} \eta_d \eta_{wg} dE \qquad (21)$$

where N_p is a function of energy given by Eq. (15) which uses Eq. (19). Eq. (21)

represents the maximum theoretical photon output from the MOF fiber considering the

photomultiplier tube and associated electronics, the number of X-ray photons, the

scintillation material, the waveguide efficiency, and the energy range of detection.

CRYSTAL GROWTH FROM THE MELT

While crystals can be grown from a variety of methods, including solution, vapor,

solid, and liquid, the liquid-solid technique is the focus of this work. Typically this

technique is called growth from the melt and is comparable to ice crystals or snowflake

formation in the winter from atmospheric water. In this case, a controlled temperature

gradient causes the formation of a solid from the molten state.

The aspects of crystal growth from the melt and technology extend into electronics

and their applications. Specifically, single crystal growth is a foundational technology.

Of which, all semiconductor technology depends. While the ability to characterize and

understand what is single crystal growth is good, the fundamental theories are either

extremely complex and involve extensive heat transfer and fluid mechanics time

dependent models, or employ simpler yet less detailed thermodynamic models.

The latter is used in this work, since the former is not only extensive but is also a

focus of modern research. To say that crystal growth is not well understood is not

entirely true, however appropriate universal theories for crystal growth have not been developed and are still a topic of research. Subsequently, reporting conditions and techniques for single crystal growth is important for comparison with theories and to develop a better understanding of crystal growth technology.

While it may be readily stated that equations exists, and are presented here, these macro scale thermodynamic relations do not generally yield insight into details of crystal growth. Instead, the equations show trends and relations between parameters which can guide the experimental techniques and values used in crystal growth. The atomic and molecular assembly of crystals can be considered a natural assembly under the conditions of minimum enthalpy. Impurities and disruptions to the minimum enthalpy conditions prevent the uniform molecular and atomic configuration from occurring. As such, the conditions which allow crystal growth must be maintained within narrow margins for single crystal growth [31-33].

For crystal growth from the melt, the liquid to solid thermodynamic conditions are used. The thermodynamic equations involved are [32]:

$$G = U - TS + PV \tag{22}$$

where G is the Gibbs free energy, U the internal energy, T is temperature, S is entropy, P is pressure, and V is volume. The differential form of Eq (22) is

$$dG = dU - TdS - SdT + PdV + VdP \tag{23}$$

at constant pressure at a constant melt temperature, Eq (23) is:

$$dG = dU - TdS + PdV \tag{24}$$

Eq (24) can also be written

$$dG = dH - TdS \qquad (25)$$

where

$$H = U + PV \qquad (26)$$

and

$$dH = dU + PdV \qquad (27)$$

for an isobaric process.

The free energy is considered zero at equilibrium for converting the liquid to solid phase, i.e. $dG=0$ and using Eq (25) yields

$$T_E = dH/dS \qquad (28)$$

where H is the heat of fusion, dS is the change in entropy and T_E is the melting temperature. Some general relations are the dP/dT is positive when dV is positive and negative when dV is negative. For a melting process dS is positive and Eq (25) shows dH is positive for $dG=0$, and melting is an endothermic process. The single values of dH and dS at constant pressure means only one temperature exists at melting for Eq (28) and that temperature is unique for a given pressure.

The above basic thermodynamic theory is applied towards crystal growth from the melt via Jackson's theory of interface structure [31]. Rewriting Eq (24) as:

$$\Delta G = -\Delta U_o - \Delta U_1 + T\Delta S_o - T\Delta S_1 - P\Delta V \qquad (29)$$

where ΔU_o, ΔU_1, ΔS_o, ΔS_1, and ΔV are all defined positive with ΔU_o the internal energy change from atoms attaching to the surface, ΔU_1 from other adatoms on the surface monolayer, ΔS_o the entropy change from adatoms going from liquid to solid phase, ΔS_1 due to the configuration of the adatoms surface positions, and ΔV the volume change going from liquid to solid phase – which is approximated as zero.

In evaluating the terms of Eq (29) an adatom and nearest neighbors on the solid are considered. This adatom will have n_o nearest neighbors before adding atoms with a maximum possible number of adatom neighbors, n_l. The symmetry of the crystal structure is considered such that if growth were to continue until the atom became situated in the bulk of the solid it would gain a further n_o nearest neighbors. Thus, an atom in the bulk solid having v nearest neighbors allows writing:

$$v = 2n_o + n_1 \qquad (30)$$

Defining L_o as the change in internal energy from transfer of one atom from bulk liquid to bulk solid (not to be considered enthalpy), then an atom going from bulk liquid to bulk solid will have a reduction in energy of $L_o(n_o/v)$. Also the n_o nearest neighbor atoms in the solid will have a reduction in internal energy of L_o/v, so that for N_A adatoms:

$$\Delta U_o = 2L_o \left(\frac{n_o}{v}\right) N_A \qquad (31)$$

For an adatom site there will be N_A/N nearest neighbor adatom sites filled so that:

$$\Delta U_1 = L_o \left(\frac{n_1}{v}\right) \frac{N_A}{N} \cdot N_A \qquad (32)$$

where N is the number of atoms in a complete monolayer of the surface considered. The expression for adatom phase change entropy is:

$$\Delta S_o = \left(\frac{L}{T_E}\right) N_A \tag{33}$$

where T_E is the equilibrium temperature where the phase change occurs from liquid to solid. The configuration entropy is given by the logarithm of the combinatorial arrangement of N_A atoms in N sites multiplied by k, where W is given by:

$$W = \left(\frac{N!}{N_A!(N-N_A)!}\right) \tag{34}$$

which allows writing:

$$\Delta S_1 = k \, ln(W) = k \ln \left(\frac{N!}{N_A!(N-N_A)!}\right) \tag{35}$$

which can be simplified using Stirlings approximation, where k is the Boltzmann's constant as:

$$\Delta S_1 = kN \, ln\left(\frac{N}{N-N_A}\right) + kN_A ln\left(\frac{N-N_A}{N}\right) \tag{36}$$

Lastly, considering the change in volume of the liquid to be negligible compared to the vapor, where the ideal gas equation is:

$$P\Delta V = N_A kT \tag{37}$$

and the latent enthalpy L is:

$$L = L_o + kT \tag{38}$$

Combining Eq's (29-38) gives:

$$\frac{\Delta G}{NkT_E} = -\left(\frac{L_o}{kT_E}\right)\left(\frac{N_A}{N}\right)\left[\left(\frac{N_A}{N}\right)\left(\frac{n_1}{v}\right) + \frac{2n_o}{v}\right] + \left(\frac{T}{T_E}\right)\left(\frac{N_A}{N}\right)\left[\left(\frac{L_o}{kT_E}\right) + \frac{T}{T_E} - 1\right] -$$
$$\left(\frac{T}{T_E}\right)\ln\left(\frac{N-N_A}{N}\right) - \left(\frac{T}{T_E}\right)\left(\frac{N_A}{N}\right)\ln\left(\frac{N-N_A}{N_A}\right) \tag{39}$$

and using $T=T_E$ and the expression:

$$\alpha = \frac{L_o}{kT_E}\frac{n_1}{v} = \frac{L_s}{R} \tag{40}$$

allows writing:

$$\frac{\Delta G}{NkT_E} = \alpha\frac{N_A}{N}\left(\frac{N-N_A}{N}\right) - \ln\left(\frac{N}{N-N_A}\right) - \frac{N_A}{N}\ln\left(\frac{N-N_A}{N_A}\right) \tag{41}$$

which is the relative Gibbs free energy as a function of the occupied fraction of surface sites (N_A/N).

The entropy of fusion (L_s) is found in the literature as 56 J/mol K for anthracene [34] and $R = 8.314$ J/mol K. The alkali halides have the entropy of fusion for CsI as 38 J/mol K and 36 J/mol K for NaI [35]. This yields $\alpha = 7.1$ for anthracene, 4.6 for CsI and 4.3 for NaI. Eq. (41) shows the minimum relative free energy $(dG=0)$ occurs at two points, N_A/N < 0.05 and N_A/N > 0.95 for α >4.2, so the number of added molecules on the crystal surface has two conditions. The first is for very low molecular addition, $N_A/N \approx 0.0$, and the second for very high addition, $N_A/N \approx 1$. These two extremes can be considered the minimum and maximum for addition of molecules which cause crystal growth. This crystal growth rate is taken from empirical data as an exponential function of undercooling with high undercooling producing high growth rates and low undercooling associated with low growth rates [31]. The low mass of scintillating material inside the quartz MOF allows the increased undercooling for the higher growth rate.

CHAPTER III

EXPERIMENTAL WORK

The experimental work consists of making or forming the scintillation fiber, characterizing an X-ray tube source then measuring the output from the scintillating fiber, performing sample preparation on the anthracene fiber for material characterization, and sputter coating the fibers with aluminum and PTFE. The liquid filled fiber is made using capillary action. The anthracene and alkali halide fibers are made by growing the scintillators as a crystal inside the fiber. X-ray measurements were made by first characterizing the X-ray tube then scintillation fiber output was compared to the tube characterization measurements. Anthracene sample preparation for material characterization of the crystal grown in the fiber is described. Finally, the aluminum and PTFE sputter coating technique is presented.

MAKING LIQUID FILLED FIBER

An image of the liquid filled MOF is shown in Fig. 7, purchased as SM-8 fiber from Newport Optics. The fiber is fused silica (quartz), 125 microns in diameter with 168 inclusions of 2.5 microns diameter. The liquid filled MOF was made by immersing an end of the fiber in liquid and allowing capillary action to draw the liquid into the fiber inclusions. The liquid fluoresced under UV light which allowed the filling to be observed; the liquid used, BC-517H, was a scintillation material in a low viscosity mineral oil. The low viscosity allowed filling the fiber in under ten seconds.
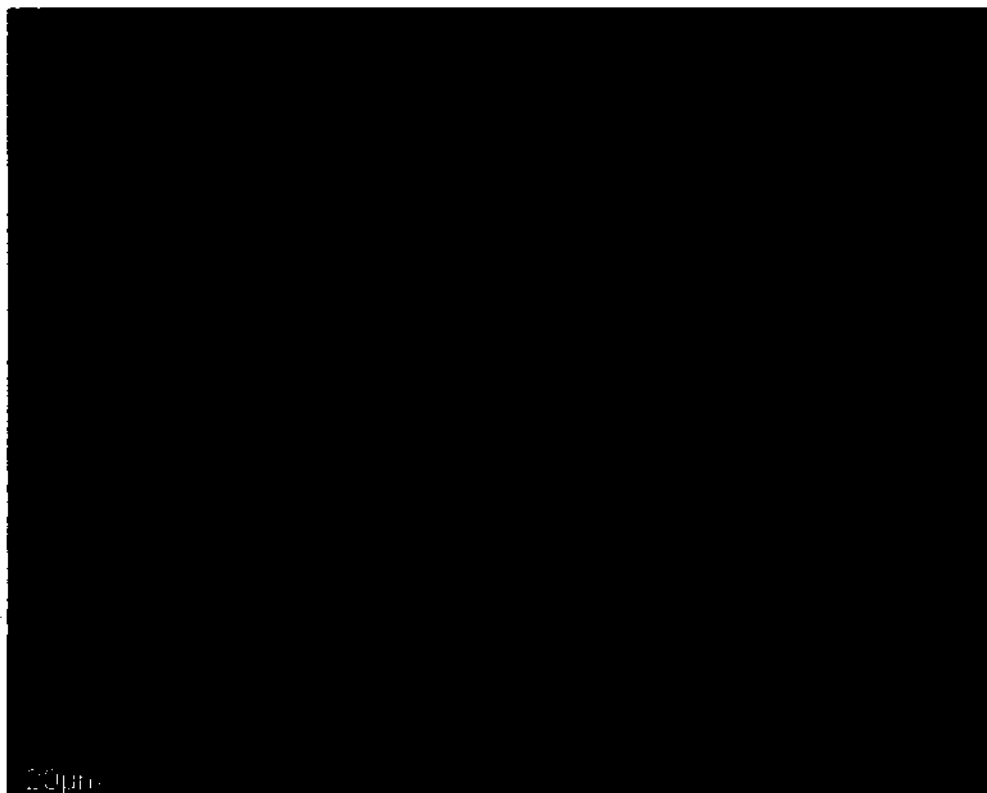
Figure 7. Shown is a SEM image of the fiber used for liquid filled MOF. Each hole, or inclusion, is 2.5 microns in diameter with 168 inclusions in the fiber. The fiber outside diameter is 125 microns.

However, as an enhancement, the fiber was subsequently inserted into a 25 G needle of a 1 mL syringe filled with BC-517H liquid. The fiber was then held in the needle while pressing on the syringe plunger. This action provided a positive pressure gradient in addition to the capillary action to fill the fiber. It is noted that capillary pressure is more than the pressure exerted by the hypodermic syringe, so this technique is marginally better than capillary action with no pressure gradient.

The handling of the liquid filled fiber was important. The capillary action filling the fiber also allowed liquid to leave the fiber. This lack of complete filling was difficult to eliminate due to this capillary effect and was typical.

A 385 nm UV lamp was the source to illuminate the liquid in the fiber. The liquid fluoresced at a wavelength of 425 nm for easy viewing with normal vision or using an optical microscope. The visible fluorescence of the liquid in the microstructured fiber allowed complete filling by visual inspection.

After filling, the fiber was immediately placed in a bare fiber connector attached to the PMT module. Scintillation visible light output was faintly visible during exposure to X-rays due to non-guided photons. The 425 nm wavelength emission from florescence also occurs during scintillation during exposure to X-rays in the BC-517H liquid.

MAKING ANTHRACENE FIBER

The experimental arrangement is shown as a diagram of the furnace cross section in Fig. 8. A tube furnace is used with upper and lower separately controlled temperature zones and contains a fiber process chamber. Inside the process chamber are anthracene and microstructured optical fiber. The process chamber is attached to a translation stage to allow movement from the higher temperature melt zone to the lower temperature freeze zone.

Ball valve vacuum rated → Vacuum pump or argon gas

Process chamber tubing, 6.35 mm OD x 0.89 mm wall x 762 mm – ¼" x 0.035 x 30" 316 stainless

Process chamber, 19.05 mm OD x 1.64 mm wall x 216 mm – ¾" x 0.065 x 8.5" 316 stainless

Insulation

Tube furnace

Quartz tube, 50.6 mm OD x 3 mm wall x 610 mm – 2" x 1/8" x 24"

MOF

Furnace upper melt zone, $T=T_m$

Insulation for transverse gradient

dT/dx

Anthracene holder

Furnace lower freeze zone, $T=T_f$

Insulated cap

Figure 8. Diagram of furnace configuration for growing anthracene crystals inside microstructured optical fiber (MOF).

In this arrangement, the furnace lower opening is capped to prevent any chimney effect and the upper opening has insulation pieces around the chamber tubing to help provide thermal stability. A quartz tube is also in the furnace between the chamber and the heating elements to reduce temperature fluctuations at the chamber. Insulation is placed symmetrically placed on two sides of the quartz tube circumference to enhance the longitudinal temperature gradient (dT/dx) and allow for a radial temperature gradient.

The furnace temperature is controlled via feedback from thermocouples placed in the heat zones. Initially, these were palladium thermocouples but were converted to K-type for better accuracy in the 30-300 °C temperature range. The temperature controllers were programmable with ramping capability. However, the best results were found operating in the on-off mode.

The fiber process chamber holds the fiber and anthracene in a controlled environment inside the furnace. A way to introduce the fiber and anthracene into the chamber is necessary along with retraction without damaging the fiber. Additionally, a vacuum and inert gas system is necessary to ensure the anthracene will not react with moisture or oxygen when molten.

Initial designs used brass pipe to construct the chamber. Consistently poor results were found with a brass pipe chamber. Plain steel pipe was used with somewhat better results. Considering the techniques for large crystal growth, it appeared that higher thermal conductivity materials were not suitable for the range of speeds and temperatures used for crystal growth. Subsequently, stainless steel was used which provided the best results.

Based on this trend, it was rational to consider quartz for constructing a chamber. However, issues with suitable wall thickness, tube end sealing, inserting and retrieving the fiber without damage were not resolved. As such, quartz was not used.

The geometry of the chamber and wall thickness were selected to fit within the furnace and allow holding the fiber and container for anthracene. The length of the chamber was chosen to fit in the lower freeze zone of the furnace. A tube from the top of the chamber extended out of the furnace and was connected to a linear translation stage for movement of the chamber from the melt to freeze zones. The tube end had a fitting for connecting a gas line to the chamber for vacuum evacuation and back-filling with high purity argon gas.

The vacuum and gas filling portion of the system consisted of copper tubing with vacuum rated ball valves attached to a rotary vacuum pump. A calibrated thermistor vacuum gauge was in this system to provide an indication of leaks during evacuation and allowed consistency in evacuation pressure. The vacuum system was evacuated between $2x10^{-2}$ and $5x10^{-2}$ Torr before back-filling with argon. The back filling with argon was done immediately before energizing the heater and beginning the melt.

Several notes were made regarding the vacuum system construction. The initial tubing was vacuum rated Tygon. This showed less vacuum capability compared to solder joint copper tubing. However, a small section of Tygon tubing was used at the chamber connection to allow more flexibility for the chamber movement.

The chamber tubing was 0.75" OD. The tubing from the top of the chamber was 0.25" OD with .035" wall 316 series stainless steel. All tube fittings were 316 series stainless steel swage compression type. Also, the chamber wall thickness was initially 0.035" and increased to 0.065" to provide improved sealing under vacuum. Before increasing the chamber wall thickness, a gradual increase in vacuum would occur with each re-use of the chamber.

The upper fitting for the chamber included an adapter for 0.75" to 0.25" tubing. The lower fitting was a cap. The upper fitting was installed and never removed. The lower fitting cap was removed then reinstalled for each new fiber processed.

The microstructured optical fiber was held inside the chamber using a modified brass fitting which also provided a significantly greater quantity of anthracene for use by the fiber. This significantly larger volume approximated a large vat of anthracene for the

fiber to draw up using capillary action when the anthracene is melted. This vat for the anthracene fiber also supported the fiber and when in the chamber.

The vat was constructed using a 1/8" flared pipe plug and a 1/8" flared pipe cap. The cap was machined using a #80 (343 micron) drill bit for a hole to accommodate the 125 micron diameter fiber cladding and coating. The plug portion was drilled out to a 3mm diameter and the length increased to 8mm.

The plug portion was filled as completely as possible with anthracene flakes before screwing the cap in place. The threads between the cap and plug were sealed using industrial Teflon tape, suitable for 500 °F (260 °C) temperatures. The MOF was cut and cleaved with the newly exposed end inserted through the cap hole and into the anthracene. A pliable sealant, also with a 500 °F temperature rating was applied to seal the fiber to the cap.

The chamber was attached to the vacuum system and pumped down for 48 hours. This time was based on calculations to evacuate the vat through the microstructured fiber. The vacuum was generated with the chamber in the furnace ready for melting the anthracene.

After being evacuated, an argon gas blanket at 2 Psig (1.1 Atm) was introduced into the chamber. This inert gas prevented any other gas from entering the chamber and stopped any thermal vacuum deposition effects. Without the argon gas blanket under low pressure conditions, thermal transport would pull molten anthracene from the end of the fiber where it would be deposited in the lower cool zone. Because the anthracene contracts upon cooling, this thermal vacuum transport was disruptive to the crystal

growth of the fiber near the end. Additionally, when crystal growth was attempted under vacuum, the lower (cool) section would be filled with thin anthracene crystals which required careful cleaning of the chamber.

The furnace upper melt zone was set at 230 °C and the lower freeze zone at 70 °C. The furnace was held at the melt temperature for one hour after energizing to ensure complete melting and capillary flow of liquid anthracene into the microstructured fiber. Upon melting, the chamber was translated at a fixed rate for 230 mm.

The translation speed was programmable and could be varied from a low of .1 mm/h up to 90 mm/h. Additionally, the translation speed could be changed over a set length. The translation speed could be held constant or ramped over a specific length. This feature enabled a variable translation speed.

The MOF acrylic coating provided by the manufacturer was left on the fiber during processing. The condition of the coating and its ease of removal provided additional evidence of the argon purity and lack of oxygen or water vapor in the chamber. The coating helped protect the fiber during removal from the chamber and was chemically swelled upon removal. The swelling of the coating allowed removal with minimum contact to the quartz which introduced defects aiding breakage. In general, the optical fiber benefits from a coating to prevent breakage during handling.

MAKING ALKAI HALIDE FIBER

The experimental apparatus and technique for making anthracene fiber was applied to the alkali halide scintillators. The coating on the MOF was removed for alkali halides due to the higher temperatures. The upper melt zone temperatures were set above the

known melting points of CsI, at 621 °C and NaI at 651 °C [19]. Table 3 lists the upper

melt and lower freeze zone temperatures with the translation speed. The lower freeze

zone temperatures were 200 °C below the melt zone, which was the lowest stable

temperature for the furnace. The translation was downward in x-direction as shown in

Fig. 8. Upon completion of the crystal growth, the fibers were placed in a desiccant

chamber due to the hygroscopic nature of NaI(Tl) and CsI(Na).

Table 3. Furnace temperatures and translation speeds for alkali halides.

Alkali Halide	Upper zone Temperature (°C)	Lower zone Temperature (°C)	Translation speed (mm/h)
CsI(Na)	650	450	25
CsI(Tl)	650	450	35
NaI(Tl)	700	500	25

Fig. 9 shows an image of the MOF used. The fiber has 138 inclusions, or holes, and

each is 2.5 microns in diameter. The fiber outer diameter is 125 microns which allows

connection to standard fiber optics.

The CsI(Tl) and CsI(Na) were provided by a scintillator manufacturer. The NaI(Tl)

was formed by taking a pre-made crystal and using a mortar and pestle to crush the

crystal inside a dry box. The alkali halides were stored in a dry box.

Figure 9. SEM image of the microstructured optical fiber taken at 30 keV. The 138 inclusions are 2.5 microns in diameter and extend the length of the fiber. Scintillation materials are grown in these inclusions.

X-RAY MEASUREMENTS

An X-ray tube allowed exposure of the fiber to ionizing radiation and measurement of the light output. This was done in two steps, an initial evaluation and a systematic study. After initial evaluation, it was clear that X-rays could be detected. Next, a set of measurements were made to characterize the X-ray tube. This characterization would allow determining the efficiency of the MOF for detecting X-rays.

The experimental setup consisted of an X-ray tube, an X-ray spectrometer suitable

for the energies measured, X-ray detecting MOF and visible photon detection electronics

for counting the photons. These components were enclosed under a leaded Plexiglas

housing to prevent exposure to X-rays while still allowing some flexibility in seeing the

setup. During typical operation, this enclosure was covered in black-out cloth to

maximize the sensitivity of the photomultiplier tube. Controls for the X-ray tube and

electronics were outside the enclosure. The X-ray spectrometer was placed in front of the

tube for characterization, then removed and replace with scintillating MOF. The

placement and orientation of the fiber were to duplicate the conditions at the detector to

allow a comparison with the fiber analysis.

X-ray tube characterization was performed for a Moxtek 40 kV 4 watt tube using an

Amp-Tek X-ray spectrometer with a CdTe detector over the energy ranges of 10 to 40

keV. A collimator was used with the CdTe X-ray spectrometer to collect photons over

the energy range of 10 to 40 keV. The spectrometer was calibrated using an americium

241 isotope. The collimator contained two tungsten disks, 5 mm thick with apertures of

100 microns and 200 microns in front of the detector. These apertures restricted X-ray

photons falling on the detector and provided a linear alignment of the spectrometer with

the X-ray tube.

The arrangement of the experimental work to measure X-ray photon counts from the

tube is shown in Fig. 10. The X-ray tube and controller is at one end. A distance of

5mm between the tube and collimator end was chosen to ensure adequate photon

interaction with the fiber and ease of repeatability. The X-ray spectrometer collimator is

aligned using the small optical table bolt hole pattern and the tube holder.
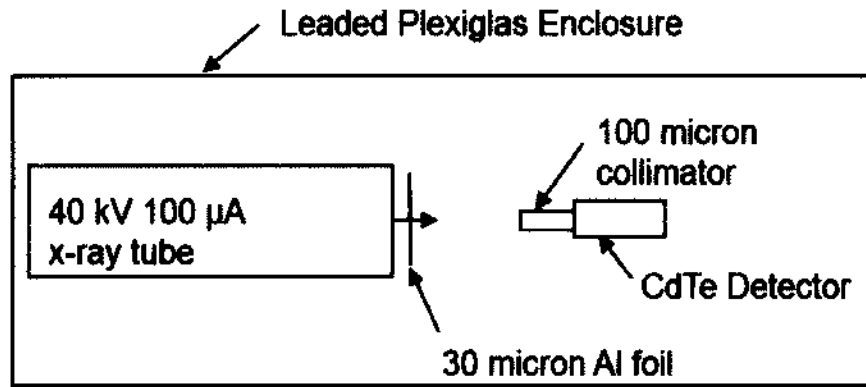
Figure 10. Experimental setup for characterizing the Moxtek 40 kV tube.

The maximum X-ray counts corresponded to having the tube at maximum voltage and current settings for maximum power. The current settings were kept at the maximum value with the voltage changed. The voltage was changed in increments of 5 kV starting at 10 kV and ending at 40 kV.

The Amp-Tek spectrometer was model XR 123 and used a USB interface connected via a Windows XP computer to collect data. An americium 241 isotope with a characteristic gamma energy peak at 60 keV was used to calibrate the spectrometer software. This calibration data was saved and used for subsequent energy spectrum measurements of the Moxtek X-ray tube. The americium 241 isotope was used because of its energy range and availability in home fire detectors.

The X-ray photon counts at the 5 kV voltage settings provided curves with photon counts at electron volt energies. The number of photons at each energy setting was used to construct a tube energy function for calculating the maximum photon output of liquid filled MOF scintillating fiber. The energy range, while experimentally collected, could in principle be calculated using software such as MCNP5 for a specific X-ray tube

configuration. However such modeling of the X-ray tube would not be as accurate as the measured energy and photon counts.

Photodetector assembly and fiber optic coupling

Photomultiplier tube:

A photomultiplier tube (PMT) was used for the BC-517H liquid, anthracene, NaI(Tl) and CsI(Na) with a wavelength sensitivity in the range between 390 and 650 nm with peak efficiency near 425 nm. This range of operation was chosen for the scintillating MOF output peak near 425 nm as shown in Table 2. The PMT was housed in a module with associated electronics for photon counting. The PMT for this range of wavelengths has a bialkali anode and the highest sensitivity due to the lowest dark current noise of any detector assembly. The PMT was configured with a FC fiber optic adapter. Fig. 11 shows the experimental configuration for measurements.
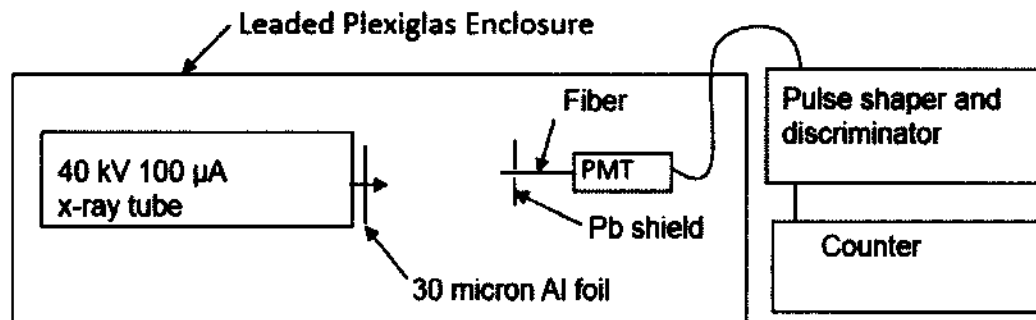
Figure 11. Experimental setup for measuring fibers with a photomultiplier tube (PMT). Scintillators with emission near 425 nm were measured with the configuration.

The bialkali anode provided peak quantum efficiency at 425 nm with an efficiency near 25%. This efficiency is linked to the anode current and voltage potential, which varies the photon detection sensitivity and noise. Cooling the PMT and associated

electronics has been one technique to increase sensitivity, but it does not change the quantum efficiency of the bialkali anode coating. The coating uses the photoelectric effect to convert photons to electrons with a fixed efficiency. Subsequent amplification of these electrons is done in the tube and noise associated with this amplification can be improved using cooling to reduce dark current in the tube electronics.

Fiber was coupled to the PMT module using a bare fiber adapter. The fiber adapter requires clean fiber for use. Cleaving the fiber provides a square end, but is not a requirement. The end of the fiber inserted into the adapter transmits light to the PMT detector.

The PMT is light sensitive and the bialkali anode coating will retain photoelectrons from exposure to light. Any exposure of the PMT tube to stray light requires operating under dark conditions to remove unwanted electrons, which appear as noise, from the bialkali anode. The PMT module was normally kept away from light to minimize noise and reduce the dark sensitivity recovery time required after exposure to stray light.

During X-ray exposure, the enclosure was covered in black-out cloth. This cloth was a heavy vinyl used for projection screens. Stray light from overhead fixtures was easily identified from the PMT module output. Stray X-rays affecting the PMT also required consideration.

The stray X-rays were a noise source that was minimized by wrapping the PMT and fiber optic coupler in lead sheet. Additionally, a lead shield with a slit for the optical fiber was placed in front of the PMT module to further reduce noise. The noise described is the PMT signal from interaction with X-rays. This noise was subtracted from the

measurements for comparison with theoretical output calculations and efficiency. Normally, the signal from the PMT combined with the output from the scintillator is considered the PMT-scintillator output in a scintillation detector instrument. A threshold value of 0.9 V was used on the counter to remove false triggering signals.

Photon counting module assembly:

A photon counting module (PCM) was used for the CsI(Tl) alkali halide fiber due to the higher quantum efficiency of the detector near the 550 nm wavelength. This module was similar to the PMT module in that a FC fiber optic coupling allowed attaching the scintillating fiber to the module. A bare fiber adapter held the CsI(Tl) MOF attached to the photon counting module. The PCM was kept away from light to minimize noise in the same manner as the PMT to maintain a consistent method for measurements, although the PCM does not have the same dark sensitivity recovery time requirements as a PMT.

A lead sheet was placed over the module to reduce noise from stray X-rays. A separate shield with a slit was used in front of the photon counting module in the same way it was used with the PMT. The PCM was less sensitive to stray X-ray noise than the PMT, due to the smaller diameter (180 micron) of active avalanche photodiode surface. Fig. 12 shows the experimental configuration for these measurements. A threshold voltage for the counter was set a 1.1 V to remove false triggering signals.
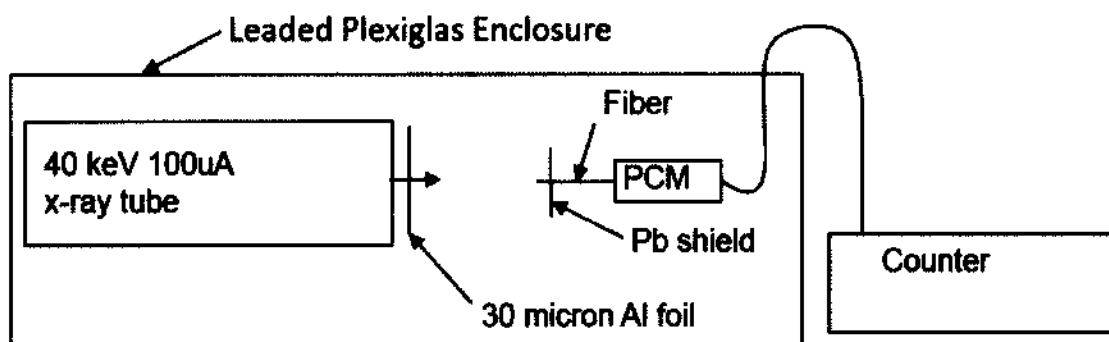
Figure 12. Shown is the experimental arrangement for measuring the CsI(Tl) fiber with a photon counting module (PCM).

PREPARATION OF ANTHRACENE CRYSTALS FOR CHARACTERIZATION

The anthracene crystals grown in the microstructured fiber were successfully characterized using three primary techniques, luminescence spectrophotometry, Raman micro spectroscopy, and X-ray diffraction. These techniques required some level of sample preparation for analysis. Two unsuccessful characterization techniques attempted were chemical and electron beam diffraction. The chemical characterization technique was unsuccessful because of the quantity needed but the electron beam diffraction was unsuccessful because the electron beam damaged the organic crystal structure.

The unsuccessful chemical technique was differential scanning calorimetry (DSC) which needs a sample size in the milligram range; only 1 microgram/cm of anthracene was in a fiber as calculated using the density of solid anthracene and the volume in a MOF of Fig. 7. A suitable sample would take a 100 meters of fiber. The electron back scatter diffraction (EBSD) technique resulted in SEM images but no structure. This was realized when observing over multiple attempts that the fluorescence of the anthracene fibers was eliminated after exposure to a 30 keV electron beam.

A TEM sample was never successfully constructed. Multiple sample attempts including embedding the microstructured fiber with anthracene in an epoxy for cutting, embedding the anthracene in sodium silicate, embedding in an acrylate plastic intended for electron beam use, and embedding in epoxies intended for electron beam use were tried. The fundamental problem was the anthracene would not remain in the quartz MOF upon slicing. After some experience with bare anthracene fiber and EBSD, which operates in the 30 keV energy range, it was recognized that a 130 keV electron beam will likely damage the anthracene organic crystalline structure. Focus was shifted to X-ray diffraction techniques, which require a larger sample size and removing anthracene from the quartz.

X-ray diffraction is the most widely used organic crystal structure tool with a highly developed database for organic crystals. Chronologically, Raman spectroscopy was done first because the sample was easiest to fabricate, XRD second after a suitable size sample was prepared, and lastly spectrophotometry.

The Raman spectrometry was performed using a piece of anthracene microstructured optical fiber cleaved and held vertically. A UV light source placed near the fiber sample aided in using an optical microscope to locate a good anthracene location in the open face of the cleaved quartz. The microscopic focus capability of the Raman spectrometry system made characterizing the microscopic anthracene quick and relatively easy.

The time for the Raman spectroscopy preparation was not spent in sample preparation, but in determining the appropriate laser wavelength and collecting published anthracene data. The published data allowed a quick comparison with the analysis to

ensure the data collected was reasonably accurate. The 785 nm laser source was selected because it was furthest from the 350 nm range UV absorption and 400 nm range fluorescence emission of anthracene. Two polarization states were planned for analysis based on published anthracene crystal data. However, the published polarization states were for different crystal orientations and not for light polarization modes.

Sample preparation for the XRD data collection began with attempting to collect diffraction data with the anthracene in the microstructured quartz cladding. This provided unsuccessful because of the broad spectral diffraction from quartz covered the anthracene diffraction peaks other than (100). Since XRD is a surface analysis technique, this explanation of the poor results resulted in removing the anthracene from the quartz.

A HF acid etch was used to remove the anthracene by dissolving the quartz. Previous papers for large diameter anthracene have described etching away the glass ampoule from the grown crystal using hydrofluoric (HF) acid. SEM and EBSD examination required bare anthracene fiber using a HF acid etch.

The sample chosen for XRD analysis used 60 pieces of anthracene microstructured fiber of 1-cm length. This length allowed constructing a 3x10 mm region for the XRD analysis. The fibers were placed in a 30 ml polyethylene container. A 15 ml volume of concentrated (45-55%) HF acid was added to the fibers and allowed to sit for five hours.

After five hours, the HF acid was neutralized using sodium hydroxide (NaOH) granules. A neutral pH was checked with litmus paper. A resulting solution was slightly basic. The anthracene fiber strands were transferred from the neutralized solution to 30 ml of distilled water in another polyethylene container.

The transfer of anthracene to fresh water was a cleaning step. The neutralization of HF acid with NaOH reacted to form $NaF+H_2O$. The NaF was a salt which visibly clouded the water. However, enough fluorescence was available from the anthracene strands to aid in extracting them from this neutralized solution into distilled water using a pipette.

The bare anthracene was then placed on a (100) silicon wafer in a rectangular pattern to replicate a thin film suitable for surface analysis with the diffractometer. A 10 mm x 3 mm sample of the anthracene was placed on the silicon wafer near the center for the diffractometer measurement [24, 35]. Figure 13 shows an image of the anthracene fibers a 50x magnification illuminated using 385 nm UV light.

The anthracene was allowed to partially dry which allowed some manipulation of the wet strands. Upon drying, a NaF salt film covered the anthracene, but fluorescence was still visible when using a UV lamp. A XRD scan of this sample was made, with poor results. XRD as a surface analysis technique required the material on or very near the surface.

Subsequently, the anthracene sample was carefully cleaned using distilled water. Water was not applied directly to the sample, but was put on a cotton swab and which acted as a blotter to dilute the NaF salt. The resulting sample had a slight salt film but with notably brighter fluorescence for the second XRD scan. This second XRD scan provided excellent anthracene crystal data when compared to the powder diffraction data file. Spectrophotometry was then used to collect the excitation and emission spectrum of the anthracene fiber.

Figure 13. Anthracene yarn formed from 2.5 micron diameter fibers when removed from quartz matrix. A 385 nm UV lamp provided the light source with a 420 nm emission from the anthracene.

The spectrophotometry was performed using a Hitachi F-4500 luminescent spectrophotometer. This instrument works on the principle of illuminating the sample with a xenon light bulb and using a photo detector to measure the emission. Not all materials are suitable for such characterization. However, anthracene is a polycyclic aromatic hydrocarbon which has good fluorescence.

A series of spectra were collected using the F4500 to insure the correct operation of the machine and accurate data. This started with self-calibration of the machine examining the spectral characteristics of the internal xenon light source. Next, an

anthracene and naphthalene sample embedded in PMMA was used as part of a calibration set. Finally, anthracene fiber etched away from the microstructured fiber quartz was dissolved in cyclohexane and analyzed to verify the calibration.

With the successful completion of these spectral analyses, the anthracene in the optical fiber was prepared for analysis. The preparation consisted of taking a 3 cm length of anthracene microstructured optical fiber and approximately centering the end of the fiber at the bottom of a quartz cuvette. The quartz cuvette was selected because it, like the microstructured fiber cladding of quartz, had no excitation or emission spectra in the 300 to 480 nm range. The fiber was centered by placing a piece of masking tape over the open end of the cuvette and using a measuring optical microscope at 50x to find the center of the covered opening. A pin hole was placed in the tape to allow putting the fiber in the cuvette and centering the fiber at the cuvette top. This arrangement allowed collecting the excitation and emission spectra from a single fiber. The excitation spectra was collected for an emission at 420 nm with the emission spectra collected for an excitation at 350 nm.

SPUTTER COATING OPTICAL FIBER

The optical fiber with anthracene and alkali halide crystals grown within the MOF was sputter coated with aluminum. The anthracene fiber was also sputter coated with ASTM D1710 PTFE. Both sputter coatings were thin films approximately 100 nm thick on the exterior of the fiber.

The films were applied in a plasma sputter chamber with high purity argon gas. The typical gas pressures were 20×10^{-3} Torr. The sputtering used DC for the aluminum at

350 watts. The PTFE sputtering was applied using RF sputtering. An initial argon pressure between 5×10^{-3} and 20×10^{-3} Torr was applied at 250 watts power to initiate a glow. The argon flow was then reduced and shut-off after several minutes once the glow stabilized [36].

CHAPTER IV

RESULTS AND DISCUSSION

This chapter contains the results and discussion for liquid filled, anthracene filled, anthracene partially filled and alkali halide partially filled fibers. Four main sections comprise the contents of this chapter. Section 1 contains the results of technique description for characterizing the X-ray tube. Section 2 contains the analytical TIR waveguide model results for liquid filled fiber with X-ray theoretical output and experimental X-ray measurements. Section 3 contains the anthracene fiber fabrication details, crystal growth observations, characterization results and discussion, theoretical X-ray measurement output based on the TIR waveguide model, and experimental X-ray measurements. Section 4 contains the alkali halide fiber growth with the experimental X-ray measurements and discussion.

X-RAY TUBE CHARACTERIZATION DATA

The use of an X-ray tube provided several benefits. These were: the control of X-ray (Bremsstrahlung) radiation emission with a power cord and on/off switch; control of the of maximum energy and amount of X-rays in a specific direction; the ability to characterize the tube energy and amount of X-rays using an X-ray spectrometer which was repeatable and stable; the CdTe detector used in the X-ray spectrometer measured X-rays in the 10-50 keV energy range with 100% efficiency which simplified comparison with scintillating MOF measurements.

The X-ray tube photon count vs. energy data is plotted in Fig. 14. This set of photon-energy curves at varying tube voltages is valid for the path of X-rays through the collimator. This collimator orientation represents the X-ray photon path through scintillating MOF. The Moxtek 40 kV, 4W X-ray tube uses a silver target anode which results in the characteristic energy peaks in Fig 14. The tube photon output is measured using a collimator with 100 and 200 micron diameter discs in front of the CdTe detector spectrometer. These sizes are chosen to approximate the optical fiber diameter.

The spectrometer is an Amptek X123 with a USB bus interface to a Widows PC with data collection software. The calibration and characterization uses the Amptek data collection software. The plot in Fig. 14 is from this software with the axes energy (abscissa) and counts (ordinate) labels enhanced for visual clarity.

This characterization was done due to lack of data for X-ray tube photon count vs energy curves. The photon counts were used to directly compare the efficiency of the scintillator MOF by a ratio of the measured photons counted to the total X-rays counted from this calibration at the varying tube voltages. Additionally, this tube data was used in calculating the theoretical maximum efficiency.

The tube characterization progressed at five minute intervals over a series of weeks to ensure the tube stability and measurement repeatability. The CdTe detector energy calibration used an Am-241 source with the collimator removed. The collimator end was placed 0.5 cm from the X-ray tube. Careful alignment of the collimator and tube maximized the measured X-rays counted.

A 1024 channel analyzer measures the X-ray photons at discrete energies which pass through the collimator with a 100 micron tungsten disk. The energy values are interpolated from a linear calibration scale. The X-rays counted from each channel form the 1024 element array $N_{xrays}(E)$ in equation (19).
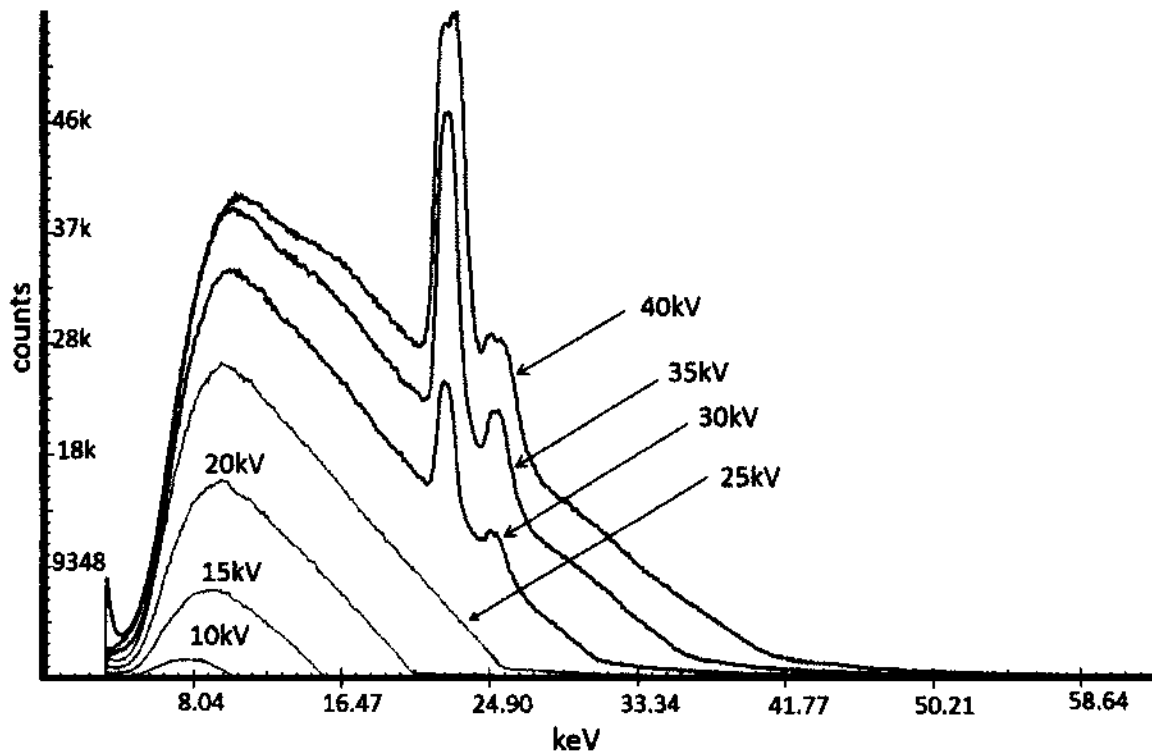
Figure 14. Tube characterization phonon count curves from 10 kV to 40 kV in 5 kV increments. The energy scale was calibrated with a 1 micro Currie Am-241 source.

The data was collected at tube voltages from 10 kV to 40 kV at 5 kV tube voltage increments. The tube current was set to 100 micro amperes. Three data sets were taken at each tube voltage and averaged. A piece of aluminum foil was placed in front of the tube to filter out low energy Bremsstrahlung ionizing radiation from the X-ray tube.

LIQUID FILLED MICROSTRUCTURED OPTICAL FIBER

A liquid was chosen as the first scintillator to use in MOF. This was due to three factors: the availability, optical properties, and ease of use. The BD-517H liquid

scintillator was purchased in a 1 L bottle with material properties provided by the manufacturer [37]. The material properties showed the index of refraction to be 1.476, as shown in Table 2, which was slightly larger than that of fused silica (n=1.458) and allowed weakly guiding TIR theory [22]. This index of refraction also allowed convergent solutions in the CUDOS multi-pole analysis software package.

The manufacturer's data provided the scintillation wavelength, given in Table 2. However, no information on the fluorescence of the liquid was available. Subsequently, the liquid excitation and emission spectra were measured using a spectrophotometer. A plot of the emission and excitation spectra for the BC-517H liquid are shown in Fig. 15. Because this is an organic scintillator, the pi-orbital structure allows the fluorescence emission using 385 nm lower wavelength UV light to be the same as the scintillation light wavelength. The main benefit of this was the ability to observe the optical fiber light emission behavior and confirm it agreed with analysis predictions. Fig. 16 shows the light emission from the end of the liquid filled MOF being confined to the liquid within the quartz.

Two software packages, CUDOS and FIMMWAVE, described in Chapter II were used to obtain modal propagation solutions, given the operating wavelength, material properties, and MOF fiber geometry. These packages determine the eigenvalue solutions for a given wavelength. For the geometry shown in Fig. 7, the analysis solutions allowed understanding how light was transmitted in the liquid filled MOF and compared with the observed transmission in Fig. 16.
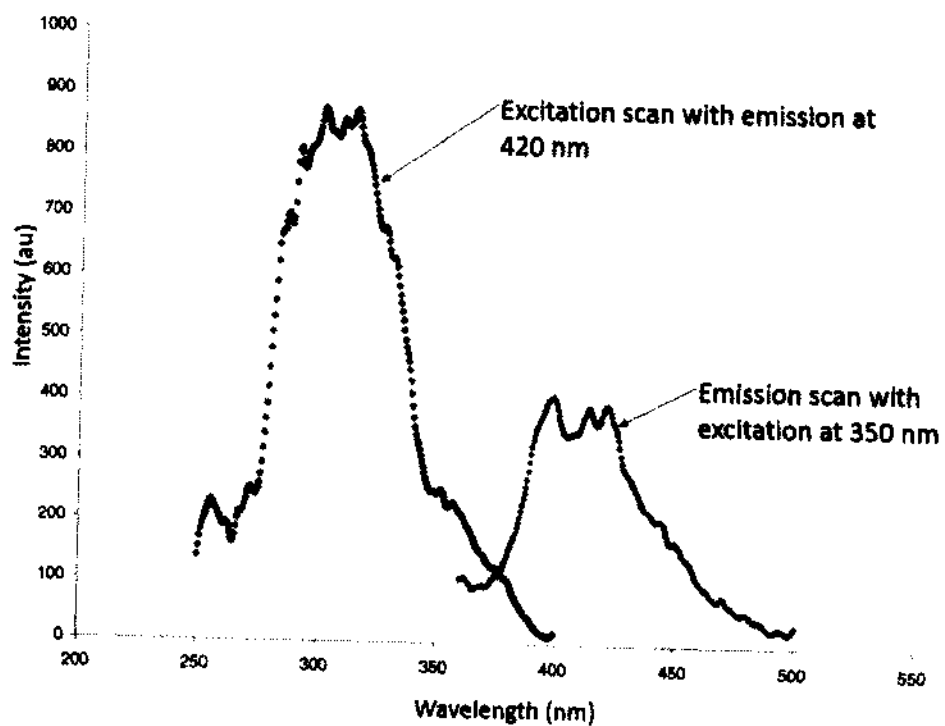
Figure 15. Shown is the excitation-emission spectrum for the BC-517H liquid.
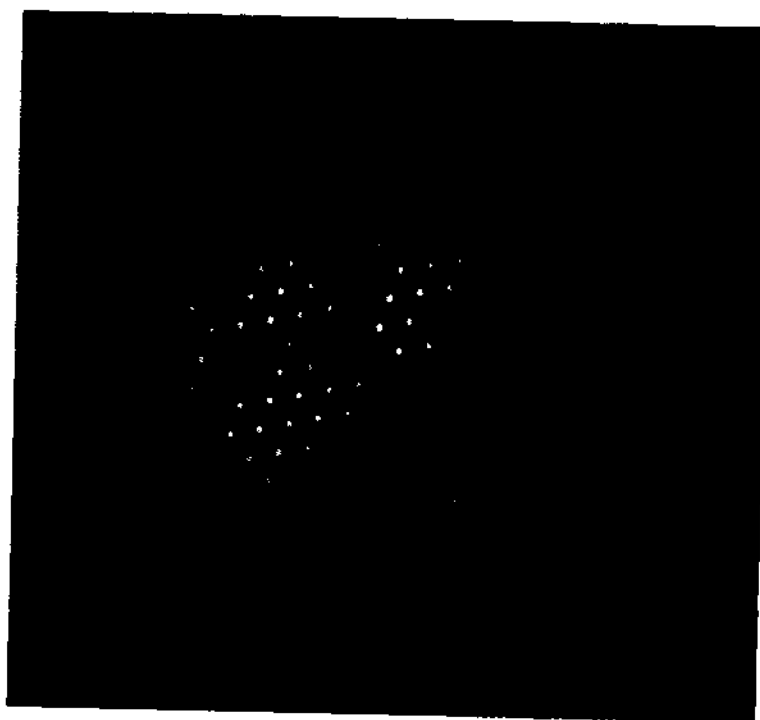
Figure 16. Shown is light emission from liquid filled MOF excited using a 385 nm UV light source. Emitted light is 425 nm wavelength, per Fig. 15. This emitted light shows guidance through the liquid.

Fig. 17 shows the CUDOS geometry generated by the software Winfield 2.00.03.15 for the fiber shown in Fig 7. This software works only with circular fibers having inclusions or holes in a geometric pattern. The quartz fiber used fit the configuration of this software. The material index of refraction was provided in an input file for both the matrix material and that of the holes. The software was written to analyze geometries having air filled holes.
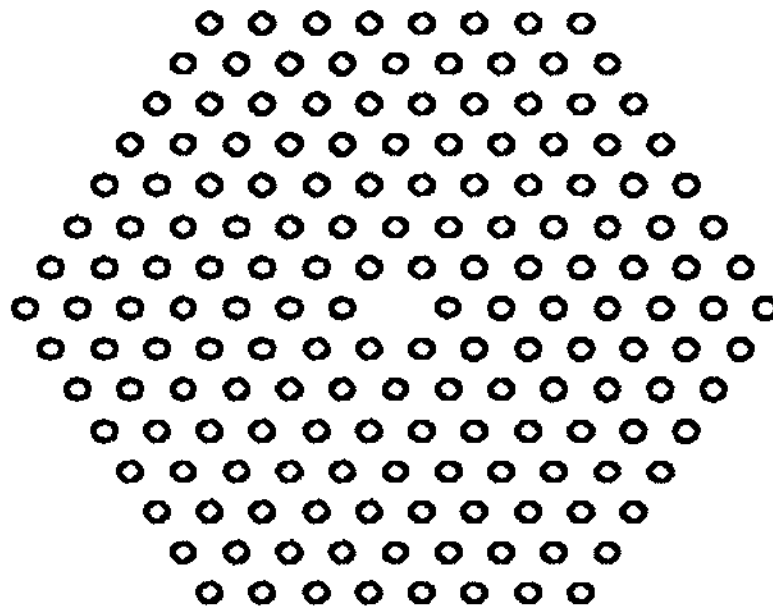
Figure 17. Shown is the geometry image from the CUDOS software. The circles represent the holes or inclusions which normally have air but are filled with BC-517H liquid for scintillating MOF. The lack of a perimeter for the fused silica MOF is associated with the multi-pole model which uses an infinite homogeneous cladding boundary condition.

Fig. 18 shows the FIMMWAVE geometry from the software. The FIMMWAVE software is a commercial package having the ability to model rectangular and circular waveguides. The modal solutions used a transmission wavelength of 425 nm with a liquid refractive index of 1.476 and the MOF refractive index of 1.458. The calculated modal solutions from FIMMWAVE and CUDOS yield propagation constants that are

real in all cases. This indicates that the slightly higher index of refraction liquid behaves as an index guiding material with the quartz acting as cladding and total internal reflection is the mechanism for the light through the liquid.
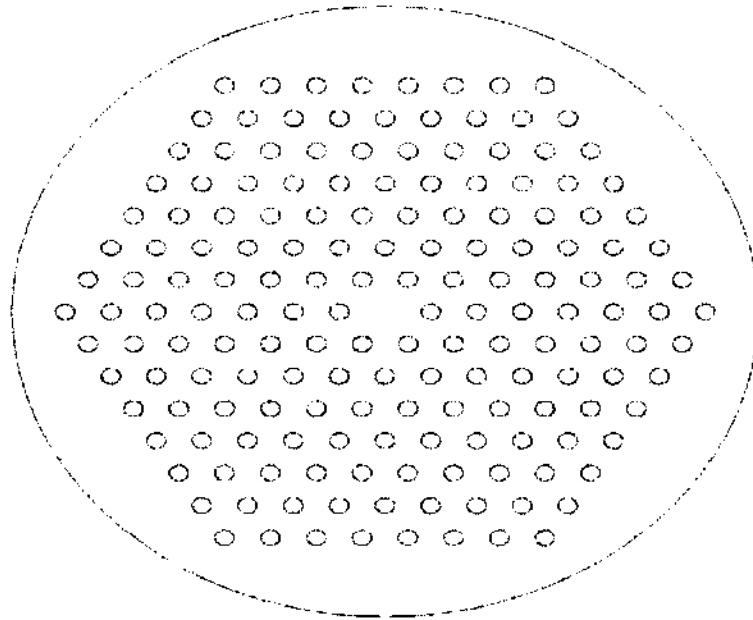
Figure 18. Shown is the geometry image from the FIMMWAVE software representing the fiber in Fig. 7. The circles represent the 168 holes or inclusions of 2.5 micron diameter which normally have air but are filled with BC-517H liquid for scintillating MOF. The perimeter for the fused silica MOF is associated with the boundary for the material refractive index.

While the band-gap and effective index solutions represent alternatives to total internal reflection, they are low efficiency light transmission mechanisms. The band-gap and effective index solutions have complex index of refraction coefficients to form solutions of the eigenvalue equations. The resulting wave is evanescent, which can be of use for some sensing applications, but has higher attenuation and power loss than guided or total index of refraction light transmission. The real guided modes in the filled MOF allow the lowest loss of light transmission in a filled MOF sensor or detector.

This same liquid filled MOF transmits light using a band-gap mechanism at longer wavelengths. However, these longer wavelengths do not apply for a scintillation detector. As such, the analysis was limited to the wavelengths of interest associated with scintillation output and resulted in guided modes associated with total internal reflection. This result was incorporated into the theory of filled MOF efficiency, described in Chapter III.

The counts from the liquid filled microstructured optical fiber measured with the theoretical output are shown in Fig. 19. The measured numbers are plotted from the experimental data. The theoretical calculation uses the X-ray counts as a function of energy from the X-ray tube calibration, shown in Fig. 9, and Eq. (9)-(21). In the case of the liquid, 7.5 photons are emitted per keV absorbed, per Table X. The waveguide efficiency is 77% and the probability of capture, P_{nc}, is 0.059%, calculated using equations (15) and (14), respectively. This low capture probability and TIR waveguide mode corresponds to the photon counts and low efficiency of the liquid filled fiber shown in Fig 20. The efficiency of the fiber is calculated by taking the ratio of the photon counts to the X-ray counts measured using the CdTe detector.
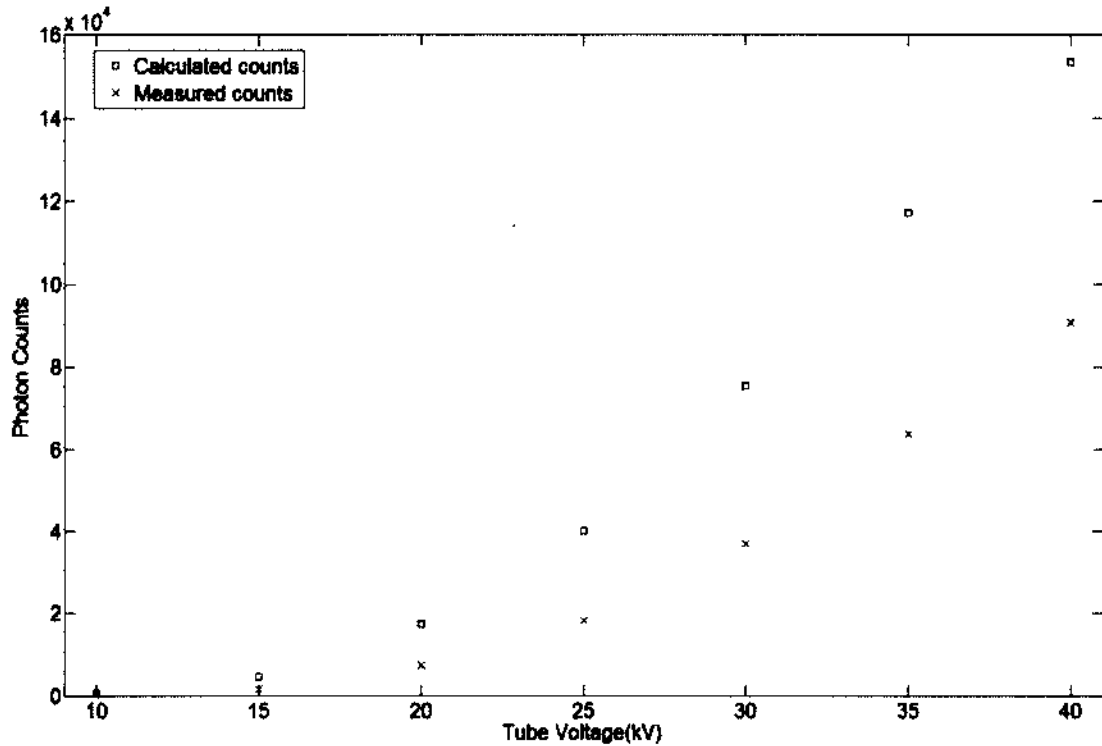
Figure 19. Measured vs maximum calculated (theoretical) counts for liquid filled fiber. The maximum theoretical counts are not significantly higher than the measured values.
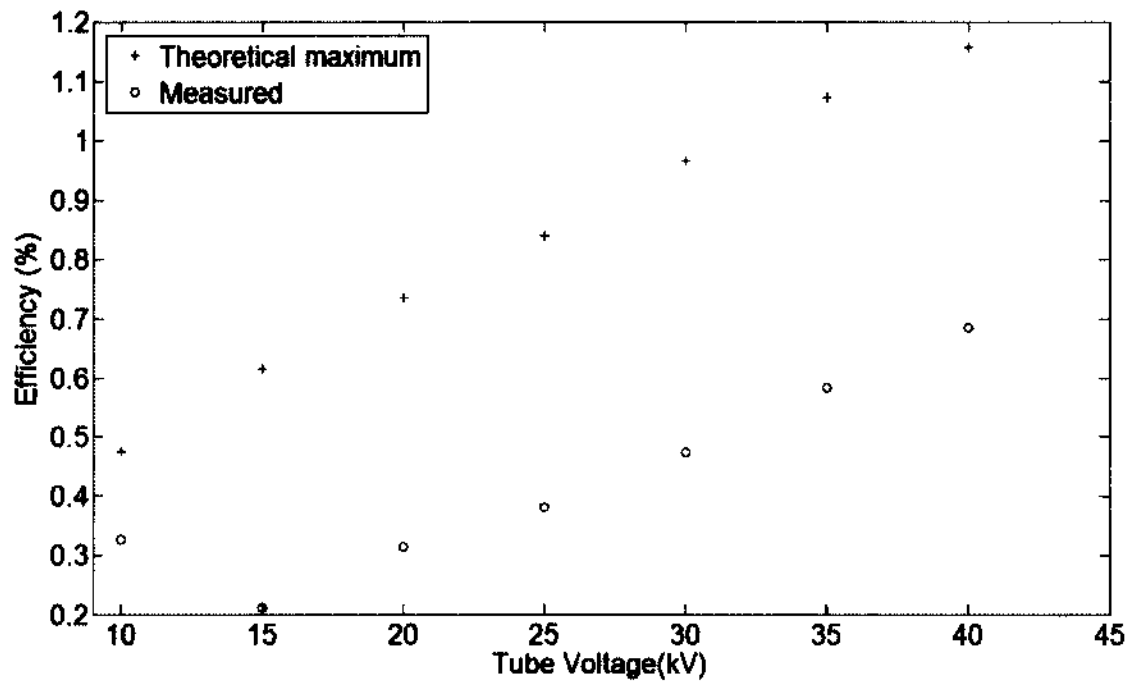

Figure 20. Shown is the liquid filled MOF theoretical efficiency and measured efficiency. The measured efficiency of the liquid filled fiber uses the data of Fig. 18.

ANTHRACENE MICROSTRUCTURED OPTICAL FIBER

The use of anthracene as a scintillator material was motived by several factors: the anthracene is a solid and easier to retain in MOF; the light output of anthracene is the highest of all organic scintillators; the decay time of the scintillation light is 32 ns; anthracene is non-hygroscopic and does not degrade in the atmosphere; the melting point of anthracene is relatively low at 218 °C [2, 18, 38]. Anthracene is a well-known scintillator available in high purity grades relatively inexpensively. The scintillation and fluorescence emission wavelength of anthracene match standard photomultiplier tube photon counting equipment. For this work, the general properties of bulk anthracene extend to the micro scale. Also, anthracene is an organic semiconductor.

Anthracene has been studied since the early 1900's for its interaction with ionizing radiation because it allows counting ionizing radiation particles by observing light pulses. Anthracene was more thoroughly studied for its scintillation properties and crystalline semiconductor behavior in the 1960's [18, 38, 39].

Anthracene crystals are grown using several techniques. These include solvent evaporation, vacuum thermal deposition, and growth from the melt. The solvent evaporation or thermal vacuum deposition techniques produce thin films of crystal. For larger crystals, growth from the melt is used. For large anthracene crystals, the Bridgman-Stockbarger technique is used almost exclusively.

The Bridgman-Stockbarger technique is simpler than the Czochraiski method and is the most common for single anthracene crystals used in scintillation. The Czochraiski method requires rotation with translation when growing from the melt in an inert

environment. However, for some semiconductors and metals the Czochraiski method produces the best crystals.

The growth of single crystals from the melt is a very complex process and is still a topic of research. Many parameters, including thermal properties of the materials, rate of temperature change, temperatures and associated sub-cooling, crystal material purity, and chemical interaction with any gasses during the melt and freezing affect the crystal growth. The melt and freezing temperatures, rate of growth, temperature gradient, and thermal properties of the ampoule and furnace are unique for different materials. For large anthracene crystals, many of these parameters are known and established. However, improvements in growth and subsequent characterization are still ongoing.

Larger anthracene crystals are most commonly grown from the melt using a seed crystal or a self-seeding technique. For large crystal growth, a purified sample of anthracene is placed in a Pyrex or quartz ampoule which is sealed. This ampoule is then carefully melted then lowered through a temperature gradient to form a controlled freezing growth of single crystal. The ampoule is removed using an acid etch to provide a single large anthracene crystal for use in scintillation measurements.

Investigating single crystal growth in optical fiber lead to organic crystals grown in the cores of glass or quartz cladding with processing properties from large crystal growth [40]. The goal of this previous work was second order harmonic generation of laser light to produce shorter wavelengths in the 400 nm range. Multiple papers were written on this subject including a patent from a Japanese electronics company [41]. The papers on second order harmonic generation used core sizes resulting in single mode transmission

of the exciting light and multimode emission of the second order harmonic generated light. It appears most of this work was not pursued further after organic LED's technology was developed, where the modern organic LED technology uses crystalline anthracene.

The incentive for pursuing anthracene cores in quartz cladding fibers came from this previous optical fiber work. The basic technique and approach to growing crystals in optical fiber all used a modified Bridgman-Stockbarger approach. The previous work demonstrated growing single crystal anthracene in the microstructured quartz was possible. The patent for organic crystal growth in optical fiber was the basis for the experimental approach. The fundamental technique used in this work was from this patent [41].

Anthracene fiber growth:

The MOF initially used with anthracene was the same for the liquid as shown in Fig. 7. Most of the anthracene characterization work used this MOF. Another MOF was used subsequent to the material characterization which was also used for the alkali halide MOF, shown in Fig. 9. The variation in fiber had no effect on growing anthracene in the MOF.

The growth experiments from the melt were conducted using a modified Bridgman-Stockbarger technique. This work was initiated at the time the liquid filled fiber was made. Initial results showed anthracene could be grown in MOF. However, it was recognized that improved fiber growth was possible.

The approach for improved growth included a stainless steel chamber which holds the MOF, anthracene, vacuum pump and associated tubing with an argon blanket used during processing. The chamber was located in a tube furnace configuration similar to the method described in [41]. The stainless steel chamber allowed drawing a vacuum to remove oxygen and water vapor. A sealed vat supported the MOF and provided a molten pool of anthracene to allow filling the quartz through capillary action. An argon blanket was introduced into the vacuum chamber before energizing the tube furnace and melting the anthracene.

The translation rate was guided by empirical trial-and-error with qualitative trends from melt growth theory. The low mass of the microstructured fiber filled with anthracene allowed using the thermal characteristics of the chamber.

The Bridgman-Stockbarger technique uses a control temperature gradient for crystal growth from the melt where growth occurs at the minimum Gibbs free energy as described in the thermodynamics theory. This temperature gradient is along the fiber in the longitudinal x-direction where crystal growth occurs. In the case for large crystal growth the heat transfer occurs primarily through the anthracene. For this work, the microstructured quartz provides the primary heat transfer path due to the relative cross section dimensions of the quartz and anthracene along with the higher thermal conductive of quartz when compared to anthracene.

The approach to determine the temperature gradient and translation speed was initially taken based on large crystal growth from the melt. However, his was found to be unsuccessful. Subsequently, the thermodynamic theory was considered and used as a

qualitative guide. However, the final values for translation speed were ultimately determined from experimental observations for void-free fiber. The chamber translation speed was set as a constant and varied from 40 down to 3 mm/h. The lower speeds were typical for large crystal growth having a low temperature gradient [42].

The reason for unsuccessful growth at low speeds was never found. The thermodynamics theory indicates growing crystals at a very low speed is possible for very low undercooling. One explanation may be that highly accurate temperature regulation is needed due to the very low micro-grams of anthracene contained in the optical fiber for low undercooling growth. Another could be that the small surface area and molecular nature of anthracene requires a translation speed much less than 1mm/h.

The results showed that speeds from 20 to 40 mm/h with the upper melt zone at 230 °C and the lower freeze zone at 70 °C produced fiber with the best optical clarity and fewest voids. Experiments showed two speed variations did not improve the fiber quality nor did speeds over 40 mm/h or speeds near 3 mm/h. These low speeds, considered typical in large crystal growth and considered in previous work did not produce continuous lengths of fibers [40, 41]. Speeds below 15 mm/h did not produce satisfactory results when using high or low temperature gradients. The highest quality fiber was drawn at speeds of 25 mm/h.

The chamber material also had a significant effect on the fiber quality. High thermal conductivity materials were not found to produce anthracene crystals longer than 1 mm. Using the lower thermal conductivity stainless steel chamber consistently and reliably allowed producing 12 cm fibers. Fig. 21 is an image of anthracene MOF with

voids labeled. A high quality anthracene fiber without voids is translucent and not visible

using incandescent light but easily inspected with 385 nm UV light.

An attribute of growth inside the optical fiber was the change in density of the

anthracene when changing phase from a liquid to solid. The anthracene solid density is

higher than liquid, resulting in contraction of the anthracene in the fiber. This effect was

used to immediately evaluate the fiber quality for further optical examination and

subsequent characterization.
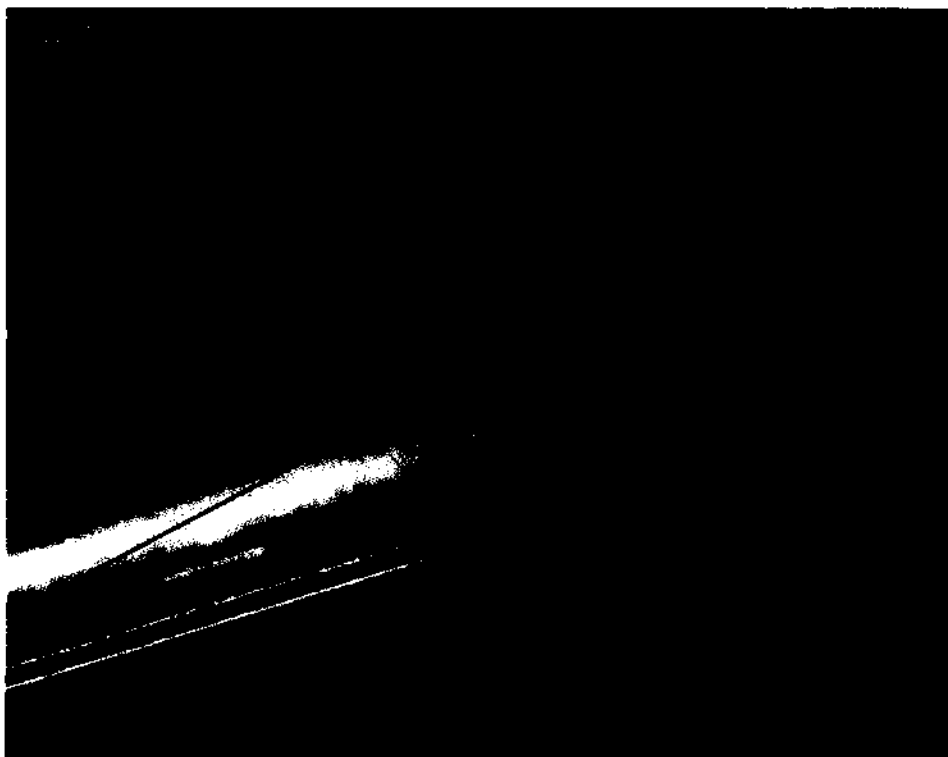

Figure 21. Shown is an anthracene MOF at 500x with voids along the growth direction.

High quality anthracene fiber in MOF is shown illuminated with 385 nm UV light in

Fig. 22. An air gap is formed in the MOF during anthracene growth from contraction due

to solidification. The air gap formed has a significant effect on the waveguide properties

and subsequent X-ray detection efficiency.

Light emission from end of fiber

Air gap caused by anthracene solidification
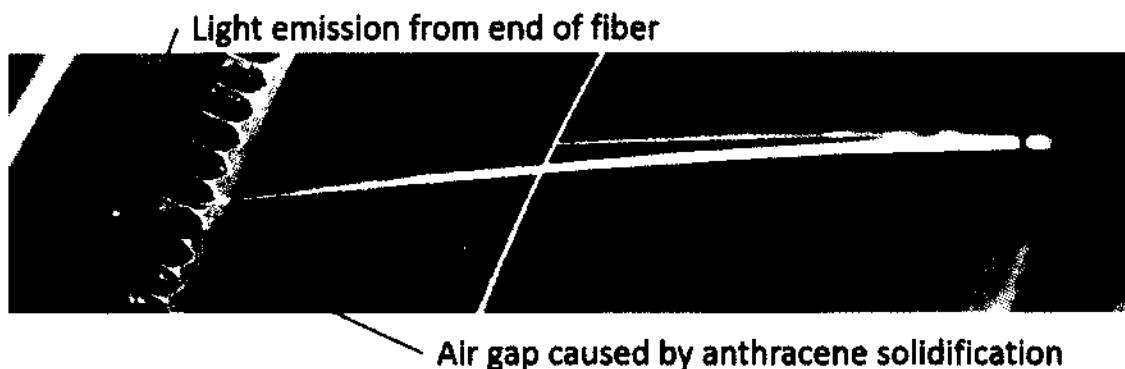
Figure 22. High quality anthracene fiber grown MOF illuminated with incandescent and 385 nm UV light showing the light emission from the fiber end and an air gap due to anthracene contraction during crystal growth.

<u>Anthracene fiber material characterization:</u>

Spectrophotometry, Raman spectroscopy, and X-ray diffraction are the characterization techniques used for the single crystal anthracene grown in MOF. The results of these techniques are compared to published data for comparison with very good agreement. This material characterization shows that anthracene grown in MOF is a high purity molecular crystal with a crystal structure similar to anthracene grown from the liquid, vapor and large crystal melt techniques.

Florescence spectroscopy

Anthracene MOF excitation-emission data was taken with a Hitachi F4500 luminescence spectrophotometer. A 3-cm length anthracene MOF was centered in quartz cuvette suitable for the spectrophotometer. The recorded excitation-emission data is shown in Fig. 23.
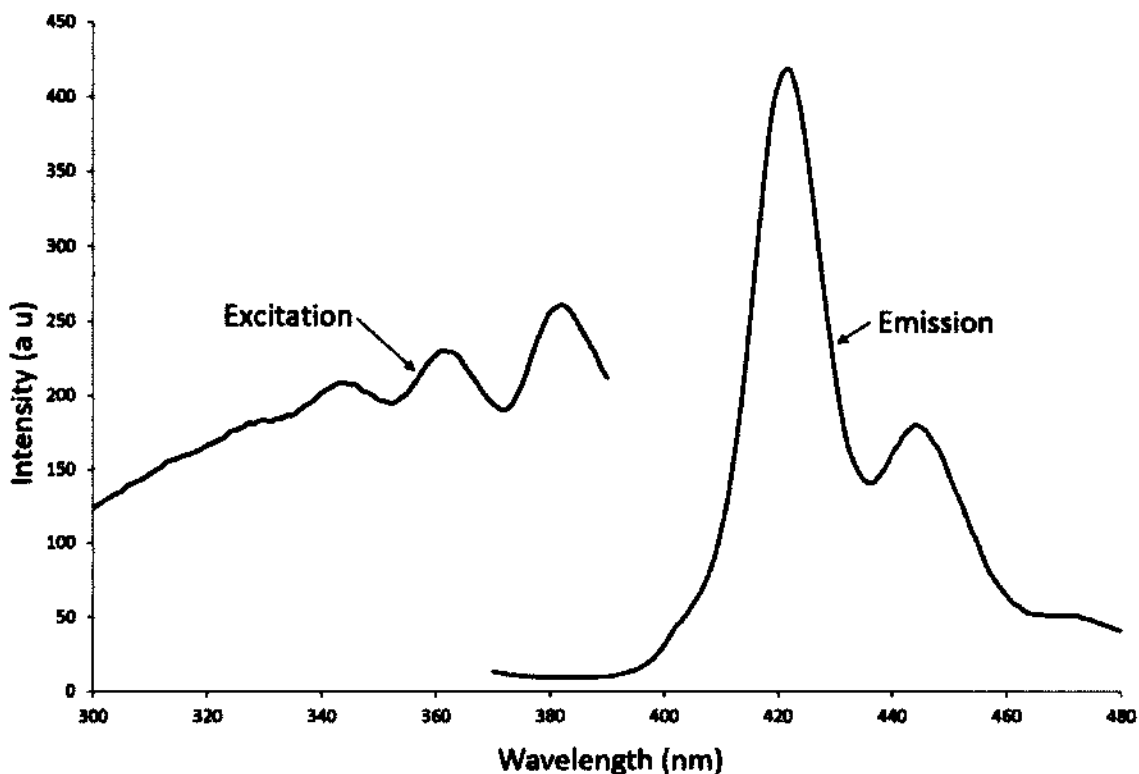
Figure 23. Excitation emission fluorescence spectrum for anthracene in quartz. The spectral emission profile agrees with microcrystalline anthracene data from Ref [38].

The excitation spectrum used a fixed emission wavelength of 420 nm with the emission spectrum collected with a fixed excitation wavelength of 350 nm. The spectral peak and shape of the emission curve agree well with the relative amplitude of microcrystalline anthracene having a main peak at 420 nm and a secondary at 445 nm [38]. The excitation spectrum shows good agreement with previous anthracene crystal data [38, 43].

Raman Spectroscopy

A Kaiser optical Raman RxN microscope was used to collect the Raman spectral data. An optical microscope incorporated into the spectrometer allowed selecting locations from the MOF end. Data was collected using a 785 nm wavelength laser and

compared with data for crystalline anthracene [44-48]. Two orthogonal polarization angles for the laser were used with both being in the plane of the MOF end. It was found that variation of the polarization angle had no effect on the wavenumber and little effect on the amplitudes of the spectrum. This lack of polarization sensitivity is attributed to no preferred orientation of the anthracene when measured at the MOF end.

Fig. 24 shows the Raman spectra with scaled data from Table 1 for anthracene crystal [44]. A comparison of the peak wavenumbers agree within $\pm$ 1 cm^{-1}. These peaks correspond to scattering from vibrational modes of the molecular solid [48]. The amplitude of the predominant peak at 1403 cm^{-1} is scaled to that in reference [44]. This scaling resulted in the peaks at 395 and 753 cm^{-1} having reduced amplitude when compared to data in [44]. However, the relative amplitude is the same with the peak at 395 cm^{-1} having the second highest peak and the third greatest at 753 cm^{-1}. The 395, 753, 1007, 1403, 1482 and 1557 cm^{-1} peaks have the greatest amplitude which corresponds to the a_g free molecular (D_{2h}) Raman active symmetry. These peaks also agree with the theoretical wavenumber calculations and published experimental relative intensity data [44, 47]. These measurements and resulting data show that the anthracene fiber has high chemical purity and the molecular structure is similar to that of anthracene crystal grown from solution.
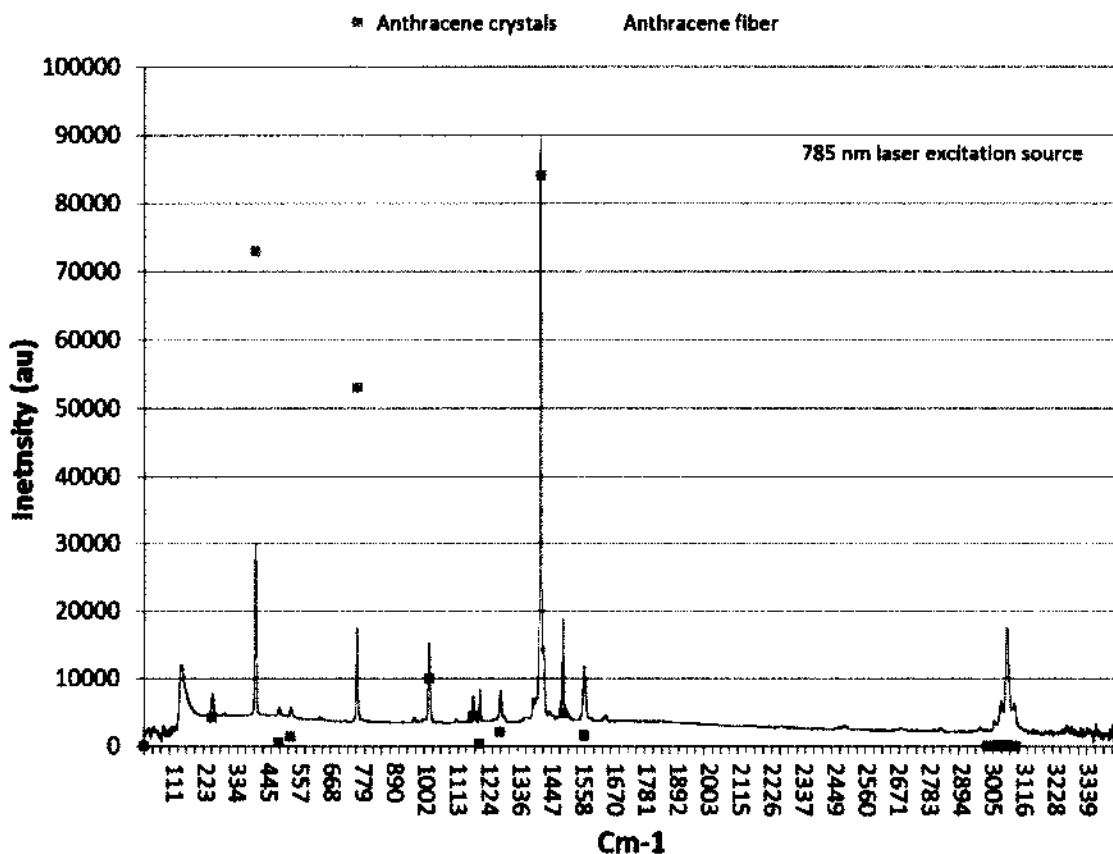
Figure 24. Raman spectra from anthracene single crystals grown in MOF. The measured wavenumbers have a ± 1 cm⁻¹ agreement with anthracene crystal data grown from solution, indicated by square markers [44].

X-ray Diffraction

A Panalytical X-ray diffractometer was used to collect the X-ray diffraction (XRD) data. The sample preparation, described in Chapter III, is configured to simulate a thin film for surface analysis in the diffractometer [49]. The peaks from the anthracene X-ray diffraction scan are shown in Fig. 25. The XRD data for anthracene has excellent spectral agreement with the XRD data for powdered crystalline anthracene within ± 0.04 degrees. The peak amplitudes differ from the powdered data because of the orientation of the anthracene strands on the silicon wafer when compared with the powdered crystal. However, the relative peaks at 19.29, 21.30, 25.28, 2 Theta angles with respective Miller

indices of (100), (-102), and (-202) agree with the powdered diffraction data [50]. The

peaks from NaF, from the HF acid neutralization with NaOH, and the (100) peak from

the silicon wafer are also shown in Fig. 25.
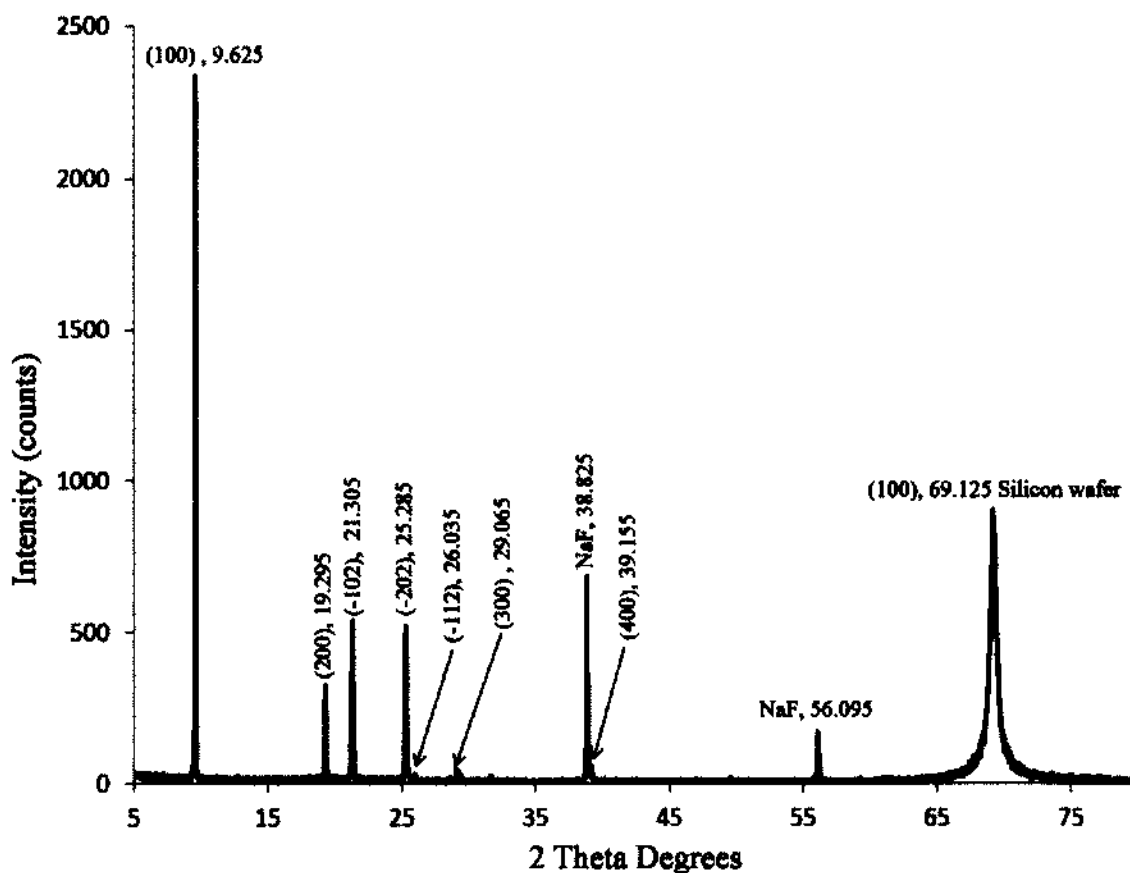
Figure 25. X-ray diffraction (XRD) data from bare anthracene fibers on a (100) silicon
wafer after being removed from quartz via etching. The (100) peak at 9.625 2 Theta
degrees corresponds to the crystal growth direction. Diffraction peak angles all
correspond to the anthracene XRD powdered diffraction data [50], sodium fluoride [54],
and silicon. The crystal orientation was used from the ICCD data file [50].

The anthracene fiber has the same crystalline structure of the bulk powdered

anthracene crystal, shown by the Bragg diffraction angles. The main peak is Miller index

(100) and in the growth direction. This main peak index is consistent with high purity

anthracene crystals grown from the vapor and solution [51, 52]. The Bragg angles allow

calculation of the crystal diffraction length. The length for anthracene grown in MOF is d_{100}=9.18 Å, which is less than the single crystal powder diffraction length (d_{100} = 9.21 Å, P21/c) and the solution grown length (d_{001} = 9.21 Å, P21/a) but larger than the vapor grown length (d_{00a} = 9.14 Å, P21/a) [49,51,52]. It is noted that the Miller indices in Fig. 25 use the P21/c space group orientation from the powdered diffraction data. However, most anthracene published data uses the P21/a space group notation [51-53]. These two space groups are equivalent for the anthracene monoclinic crystal [55].

Anthracene fiber efficiency configured as a TIR waveguide:

Initially, the fiber was grown using the MOF as shown in Fig. 7. Anthracene fiber has an air gap when grown in the MOF as a single crystal. This air gap, shown in Fig. 22, was removed by cleaving the optical fiber so the anthracene fiber configuration was the same as the liquid. The effective index for anthracene is shown in Table 2 as 1.62, which is within the range to allow applying the weakly guiding TIR theory for liquid filled fiber efficiency. Improvements in fiber growth resulted in improvements in efficiency near 100% from initial fibers grown in 2009 with those in 2012 as shown in Fig. 26.

These curves are plotted in the same manner as that for the liquid. The measured values are taken from experimental data and the theoretical maximum counts are calculated using Eq. (9) - (21). For anthracene, 16 photons are emitted per X-ray keV absorbed, per Table 2. The waveguide probability of capture is 4.9% and efficiency is 89% from equations (13) and (14), respectively. The improvement of the anthracene over the liquid is recognized to be more than the increased photon output of the two

materials. This is observed more readily in the low energy counts of anthracene fiber,

shown in Fig. 26.
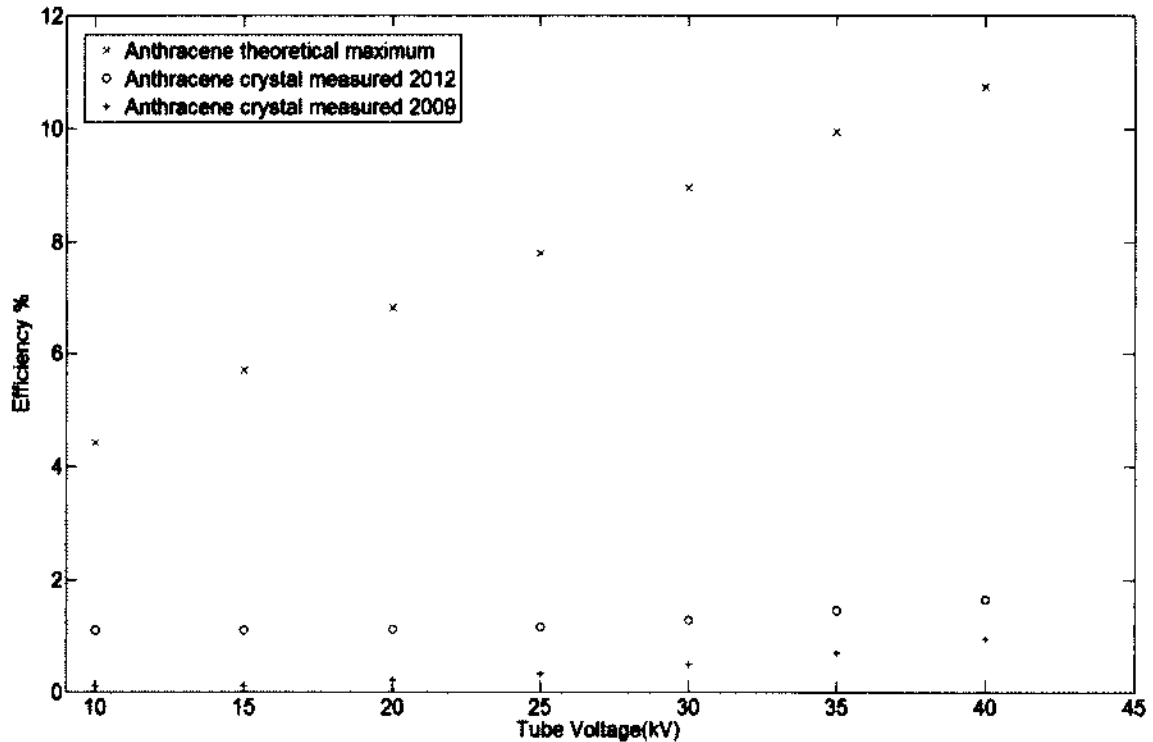
Figure 26. Shown are the theoretical maximum and measured efficiency of anthracene fibers fabricated in 2009 and 2012. The fibers are configured to use the TIR waveguide configuration of the liquid filled MOF.

Anthracene fiber improved X-ray detection efficiency:

The efficiency was measured using the setup and procedure previously described for

liquid filled optical fiber and the results are compared with those from previous

anthracene fiber efficiency [22,25]. Here, the same 40 kV, 4 W tube was the source with

a photomultiplier photon counting arrangement for the fiber output shown in Fig. 11.

The fiber configuration is shown in Fig. 9 with the FIMMWAVE geometry shown in Fig. 27.

The FIMMWAVE analysis for the new anthracene filled MOF showed the same results that all the modes are real and confined inside the anthracene. The maximum theoretical light output calculation used the weakly guiding waveguide equations and approach for the liquid filled fiber. The results in Fig. 28 show improved fiber efficiencies of 16.6% at 10 kV to 12.0% at 40 kV for uncoated MOF with an air gap as shown in Fig. 28. These values exceed the maximum theoretical light output of anthracene filled MOF.
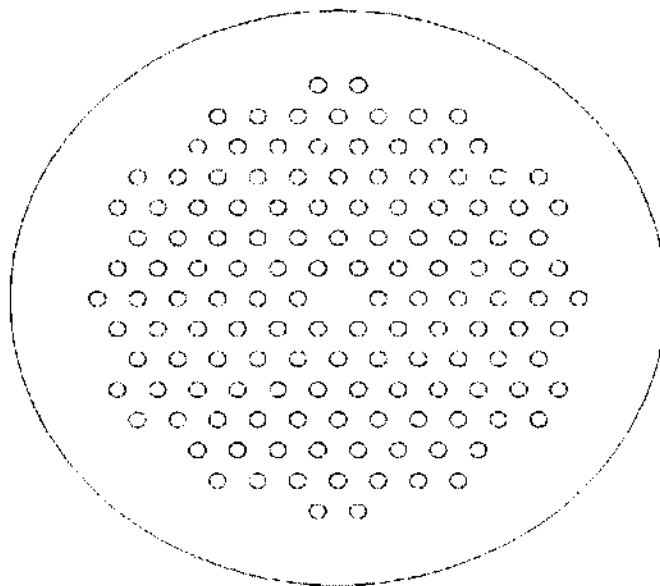
Figure 27. FIMMWAVE geometry for anthracene in quartz MOF modal analysis for MOF in Fig. 9.

The maximum theoretical output of anthracene filled MOF is based on work from liquid filled fiber where anthracene, using an effective refractive index of 1.62, is used instead of liquid [22]. A calculation of the photon capture probably in anthracene, with the quartz (fused silica) MOF acting as a cladding, is ~5% using equations (9), (12), and

(13) of Chapter II. This capture probability and representation of the anthracene in the MOF as bundle of optical fibers, each transmitting light through total internal reflection, provides the theoretical maximum output shown in Fig. 28. Since the quartz MOF acts as a cladding, any coating has no effect on the theoretical maximum light output.

The improved X-ray efficiency of anthracene MOF occurs when 425 nm wavelength scintillation light travels through the air filled MOF quartz as shown in Fig. 29. With ~5% of the scintillation light theoretically captured in anthracene, most (~95%) must travel through the quartz MOF. The capture of scintillation light through the quartz MOF allows for the improved efficiency. This improved efficiency, which involves complex three-dimensional optics, was observed for uncoated anthracene MOF. Coatings were applied and the resulting efficiency measured to aid in understanding the optics and the effect of coatings.

The use of aluminum and PFTE sputtered coatings was motivated to investigate the optical behavior of a highly reflective thin film from aluminum and a lower index of refraction thin film from PTFE, respectively. The effect of coatings with both an air gap and filled fiber shows low efficiencies, near that of uncoated filled fiber in Fig. 9. Both coatings improve handling of the fibers.

Considerations in the sputtering of aluminum and PTFE were the vacuum and UV light effects on the anthracene. It was observed that anthracene fibers removed from the quartz and exposed to a 30 keV SEM electron beam ceased fluorescing when exposed to UV light. However, anthracene continued to fluoresce after sputter coating with both aluminum and PTFE.
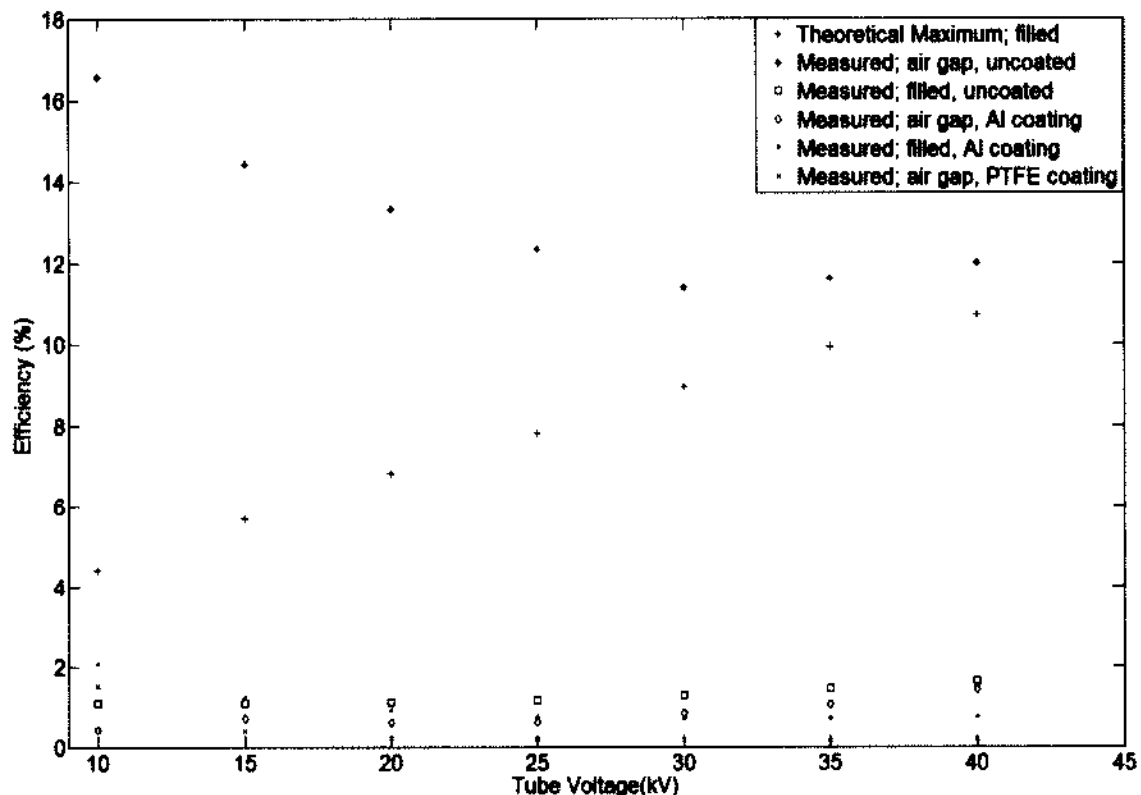
Figure 28. Anthracene efficiency from improved crystal growth with fiber having an air gap and filled. The fiber was coated with aluminum and PTFE to measure the effect of coatings on the efficiency due to the change in optics. The effect of thin film coatings produce fibers with similar efficiencies with or without an air gap.
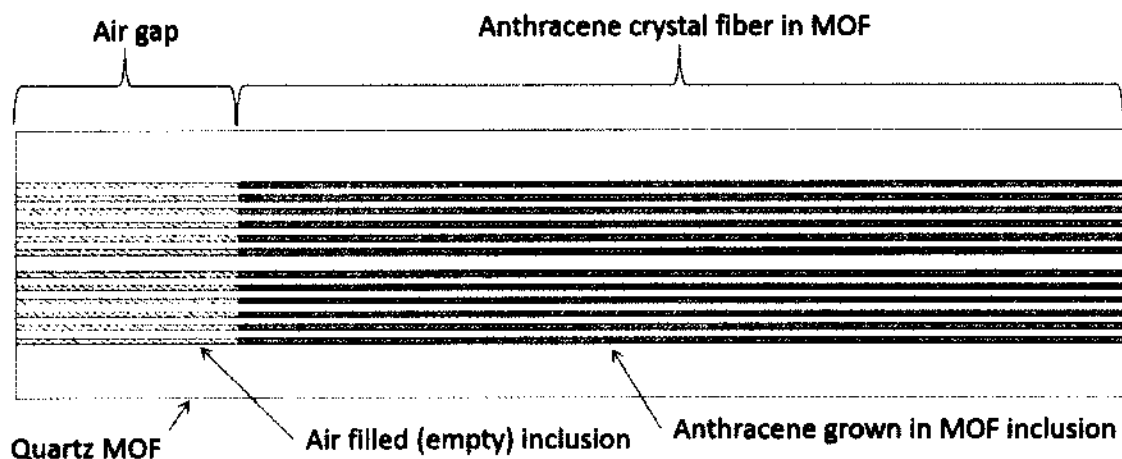
Figure 29. Cross section of anthracene fiber diagram. The anthracene, quartz, and air form the waveguide with 420 nm light emitted from the fiber end with the air gap.

Based on the experimental data in Fig. 28, the improved efficiency of anthracene fiber with the air gap and no coating is a combination of several factors: the anthracene crystal quality, the air gap formed during anthracene solidification, and uncoated (bare) quartz. Although minor imperfections in the anthracene are found in all fibers, inspection of the fiber using visible and UV light must show that the fibers are free from voids and flaws as shown in Fig. 21 and an air gap exists between the light emitting end of the fiber and the anthracene as shown in Fig. 22. These conditions must exist for a significant increase in the light output from the fiber. For example, whenever anthracene is grown in the MOF the beginning segment always has voids and must be removed; the opposite end has an air gap. These conditions provide an increase in efficiency of approximately 1300% at 40 kV and over 1600% at 10 kV when compared to filled MOF in Fig 28.

ALKALI HALIDE MICROSTRUCTURED OPTICALFIBER

The motivation for using alkali halide scintillators in MOF comes from the widespread and extensive use of these scintillators for X-ray and gamma ray detection. This is because of their X-ray stopping ability due to high molecular weight and their high light output when compared to organic scintillators.

Alkali halide fiber growth:

The alkali halide scintillators are grown inside the quartz with the same experimental apparatus used for anthracene MOF. The materials and tube furnace were selected to operate in the 600-700 °C temperature range for the alkali halides. However, it was found that the process chamber degrades from operation at these higher temperatures much faster than at the 230 °C operating temperature of anthracene.

The vat materials were changed slightly in that no tape was used on the threads and a ceramic adhesive was applied to the fiber at the cap exit to prevent the fiber from moving during processing. The resulting configuration was placed in the process chamber and evacuated using the same parameters as the anthracene fibers.

After processing, the fibers were removed and measured for output. The CsI(Tl) fiber was more tolerant of humidity than the NaI(Tl) or CsI(Na) fibers. The CsI(Tl) was able to be photographed using a 254 nm UV light source showing the 550 nm wavelength light emission from the end in Fig. 30. A diagram of the alkali halide fiber configuration and air gap is shown in Fig. 31.

Figure 30. Shown is CsI(Tl) fiber on a microscope stage illuminated by a 254 nm light source. Light emission occurs from the end of the fiber and the region with CsI(Tl) alkali halide crystal. An air gap exists inside the fiber between the CsI(Tl) crystal and end of the fiber which is formed during crystal solidification.
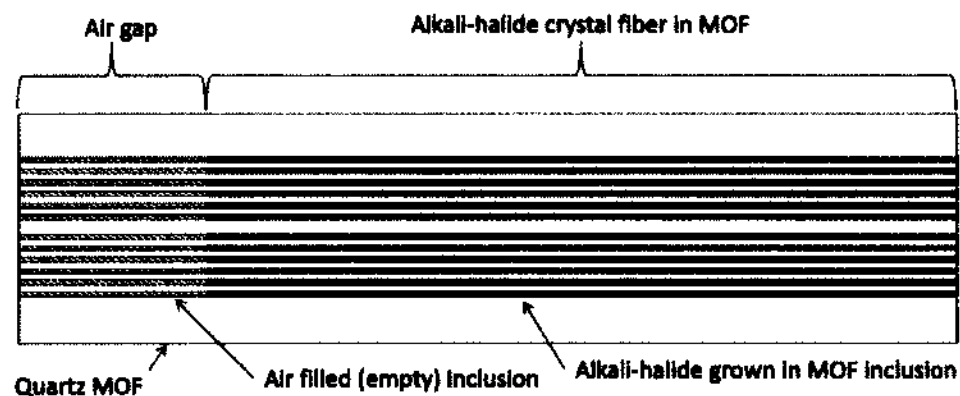
Figure 31. Cross section of alkali-halide MOF diagram. The alkali-halide, quartz, and air form the waveguide with light emitted from the fiber end with the air gap.

Alkali halide fiber characterization:

The alkali halides grown in optical fiber were not characterized, primarily because they could not be removed from the quartz. The inability to remove the alkali halides from the quartz results in extremely small samples that are contaminated by quartz when trying to characterize the material. Electron beam techniques and an attempt at electron back scatter diffraction (EBSD) measurements using anthracene have shown that charging from quartz occurs near the scintillators and prevents useable data without significant noise.

Measurement of excitation-emission with a photo spectrometer for CsI(Tl) in quartz produced poor results. This was partially due to the low fluorescence of CsI(Tl) and also the lower photon emission from the photo spectrometer Xenon tube light source in the UV-C wavelength range. Similar results were found for NaI(Tl). The CsI(Na) does not fluoresce.

No X-ray diffraction was performed on the alkali halide fibers because they are water soluble and an HF acid etch would dissolve the both the quartz and the scintillator. Transmission electron microscope (TEM) electron diffraction data could not be performed because of sample preparation. This is based on experience trying to create a suitable TEM sample with anthracene – which was never accomplished. The scintillator in the holes tends to fall out and the slicing process uses water to contain the samples, which will dissolve any alkali halide.

Raman spectroscopy can be performed. However, unlike anthracene, literature on alkali halide scintillator Raman data is not readily available. Also, Raman data allows determining the chemical purity and molecular structure of the alkali halide but does not describe the crystal structure.

Alkali halide fiber X-ray detection efficiency:

The alkali halide X-ray measurements were performed using the same experimental configuration as the liquid filled and anthracene fibers. The CsI(Na) and NaI(Tl) fibers were measured using the photomultiplier tube configuration show in Fig. 11. The CsI(Tl) fiber was measured using the photon counting module shown in Fig. 12.

The TIR theoretical model applied to the liquid filled and anthracene (filled) fibers was not applied to the alkali halides. This was because the index of refraction, as shown in Table 2, compared to quartz (n=1.4585) exceeded the criteria for the weakly guiding approximation, given by equation (9). The alkali halide fibers, configured as liquid filled (i.e. without an air gap) fibers were only slightly more efficient than anthracene, in the range of a few percent.

Fig. 32 shows the ratio of alkali halide MOF to CdTe counts as a percent efficiency vs tube voltage. The CsI(Tl) fiber output exceeds the CdTe detector at all voltages. One of the reasons for this is because 620 photons are emitted by CsI(Tl) for each 10 keV X-ray absorbed, per Table 2. Fig. 9 shows the X-ray quantity and energy at each tube voltage. The uncoated NaI(Tl) and CsI(Na) have a similar trend to the CsI(Tl) fiber. The NaI(Tl) fiber is over 70% efficient at 40 kV and over 170% at 10 kV tube voltages. The CsI(Na) is over 30% efficient at 40 kV and over 50% efficient at 10 kV tube voltages. These efficiencies depend on the detector efficiency, shown in Table 3. Higher quantum efficiency detectors, near the 420 nm wavelength range, would increase the X-ray detection efficiency of NaI(Tl) and CsI(Na) fibers.

Applying a thin film coating of aluminum on the exterior of these fibers caused a drastic reduction in X-ray detection efficiency. The NaI(Tl) and CsI(Na) fibers with an aluminum coating are a few percent efficient. The CsI(Tl) has the highest efficiency of any the coated alkali halide MOF at over 5% at 40 kV and over 20% at 10 kV as shown in Fig. 32.

The reduced efficiency is because the fiber optical characteristics are changed with an aluminum coating. The fiber transmits less scintillation light when coated with a thin aluminum film compared to the uncoated fiber. This decrease in efficiency from aluminum coated fiber demonstrates the experimental technique is sensitive to optical variations in the fibers. The decrease in efficiency is consistent with the measurements for anthracene fiber. Part of the reason to apply aluminum to the alkali halide fibers was to protect them from moisture and add strength, observe if the same optical effect

occurred with the anthracene fiber, and also to observe the sensitivity of the experimental technique to optical variations.

Theoretically, based on the two orders of magnitude greater number of photons emitted by alkali halide scintillators when compared to the number of X-rays, it is possible that greater efficiencies can be attained by incorporating scintillating material in MOF. However, the fiber optics must be carefully considered at the emission wavelengths of the alkali halide scintillators. Also, the crystal growth process has a significant effect on the X-ray detection light output.
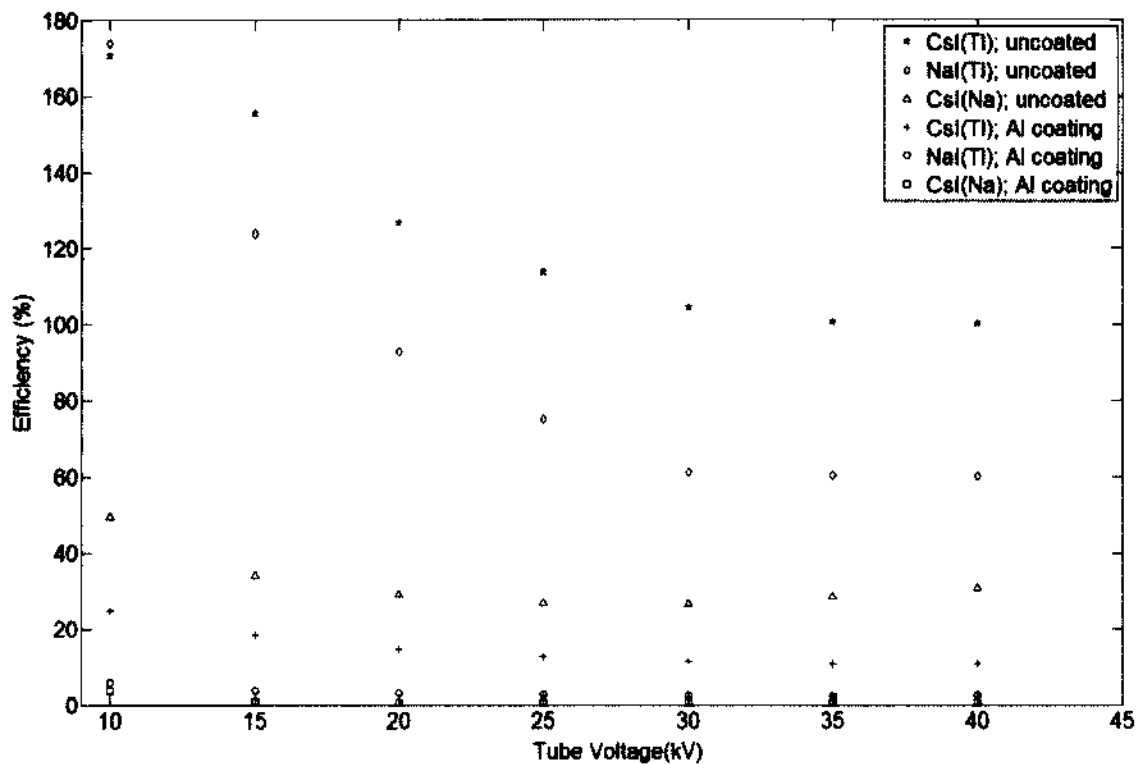

Figure 32. The X-ray efficiency of alkali halide MOF is plotted at tube voltages from 10 to 40 kV. The CsI(Tl) MOF efficiency is over 100% at all tube voltages. Addition of a thin film aluminum coating causes a change in the MOF optical characteristics and a significant drop in detection efficiency.

CHAPTER V

SUMMARY AND FUTURE WORK

The addition of scintillating liquids and solids into MOF creates an optical fiber which can detect X-rays, and in general, ionizing radiation. The use of X-rays as the ionizing radiation source was motivated by the many uses for X-rays and the ability to characterize an X-ray tube for comparison with multiple fiber configurations. This quantifiable approach to X-ray measurement also allows the development of a theoretical model using total internal reflection (TIR) for the liquid and anthracene scintillator MOFs output when exposed to X-rays. This model is based on weakly guiding optical fiber theory. As such, the alkali halide materials were not used with this model due to their higher refractive index. The Δ for the alkali halides is $\approx 18\%$, which is outside the range of weakly guiding theory, per Chapter II. The comparative Δ for liquid is $\approx 1\%$ and Δ for anthracene is $\approx 9\%$.

The current state of the art optical fibers operate based on TIR. The measurements and theoretical results presented in this work show fibers operating using TIR have low efficiency. This is primarily due to the low capture probability of scintillation light when the scintillator acts as the core of the optical fiber. This capture probability is not limited to weakly guiding theory.

The introduction of alkali halide fibers allowed measurement and quantification of another mechanism for capture and transmission of scintillation light. The configuration for alkali halide fibers with this improved mechanism was also repeated for anthracene

fibers. The CsI(Tl) fiber output results were over 100% efficiency for all energies. The NaI(Tl) fiber is over 70% efficient at 40 kV and over 170% at 10 kV tube voltages. The CsI(Na) is over 30% efficient at 40 kV and over 50% efficient at 10 kV tube voltages as shown in Chapter IV Fig. 32. This improved efficiency is related to the optics because the light must travel through the quartz rather than only the scintillator as shown in Figs. 22 and 30 with the corresponding fiber cross sectional diagrams in Figs. 29 and 31.

Two thin film coatings were applied to the exterior of anthracene fiber to investigate the change in optics. Both aluminum and PTFE coatings drastically reduced the efficiency of scintillation light collected when applied to previously measured fibers. An aluminum coating was applied to the alkali halide fibers with the same result. The thin coatings only change the visible light optics and not the X-ray interaction with the scintillator. These measurements with thin films were also useful to check the experimental technique to ensure the higher efficiencies being measured were not an error or noise.

The improved efficiency for anthracene was compared to the maximum theoretical efficiency of fiber operating using TIR. As shown in Fig. 28, the measured efficiency was over 12% which was above the maximum TIR efficiency values of 11% which indicates TIR waveguide operation is not optimal. A consequence of the higher efficiency mechanism with the alkali halide and anthracene fibers is the increased complexity of the optics. In the case of the TIR mechanism using weakly guiding waveguide theory, the mechanism for light transmission and capture can be described by the theory in Chapter II. However, the high efficiency anthracene and alkali halide fibers operate with an air gap and uncoated (bare) fiber and cannot be adequately described

using this theory. The optical propagation occurs along the longitudinal axes of the fiber and emission occurs at the end with the air gap. This indicates that light must originate in the scintillator material and travel through the quartz to achieve this improved efficiency. Since the light must escape the scintillator-quartz TIR waveguide structure, shown in Figs. 28 and 30, the probability of capture can exceed the 4.9% of anthracene. The quartz-air interface on the outside of the fiber is coupled to the quartz-air interface within the microstructure of the fiber. This transmission of light extends the state of the art from TIR optics and results in much higher X-ray detection efficiency.

A fully three dimensional technique is needed to model the light propagation through the quartz using a modal analysis. The main region of focus is the scintillator/air interface along the fiber length, considering the radial microstructure and exterior quartz/air interface. Currently, no available software can perform a modal analysis on such a geometry. A modal analysis cannot directly describe how light is captured, or the capture probability, of the improved efficiency fiber configuration. However, understanding the mode coupling between the scintillator/quartz/air and air/quartz/air regions of the fiber may help with a theoretical description for the capture and transmission efficiency of light in the fiber.

The increased efficiency of the alkali halide and anthracene fibers was found after noticing increased light emission from the end of the CsI(Tl) fiber when using UV light. Later X-ray measurements showed the increased efficiency of all alkali halide and anthracene fibers configured with an air gap and uncoated. The increase in efficiency in all cases was over an order of magnitude with the CsI(Tl) measured efficiency over 100% as shown in Fig. 32 .

The use of a coating on the scintillating MOF was motivated by not only investigating the optics, but also several practical aspects. A metal coating prevents moisture and will protect the scintillating material. A metal or opaque coating will remove noise from in the form of visible light. Additionally, a coating on the optical fiber will ease the handling and prevent breakage. However, the results show a significant decrease in efficiency when a coating is applied to the fiber exterior.

The exposure of bare quartz to atmospheric moisture degrades the strength of the fiber and allows the fiber to break easily. This same moisture is absorbed by NaI(Tl) and CsI(Na) which are hygroscopic, so a coating can eliminate more than one problem. However, the problems of moisture and fiber handling are ones which can be resolved by other approaches. The optical considerations of the air/scintillator/quartz tertiary material which shows increased efficiency is of the most interest for future work. A better understanding of the improved optics can provide a path to increased efficiency in other microstructured optical fiber devices.

From a practical perspective, even with low efficiency, the scintillating fibers may be developed to work with useful devices. The crystalline scintillator MOF is generally easier to work with than liquid filled fiber. However, liquid filled optical waveguides are fairly easy to understand and have considerable flexibility in the liquids available. The main focus of this work was to demonstrate the feasibility of scintillating MOF and explain the operation. The observation of a much higher efficiency and different optical transmission mechanism than TIR was unexpected but recognized as quantifiable.

Additionally, the fiber optic modeling can be applied to liquid and solid filled fluorescence sensors which operate using TIR optics, provided the weakly guiding approximation is valid. Research on anthracene crystals found that anthracene has more uses than an X-ray scintillator. These include, spectral florescence variations and quenching from magnetic fields with absorption and florescence spectra variations from pressure [56-60]. Thus, this work for X-ray detection using MOF can be applied to other fiber optic sensors. However, the alkali halide fibers, comprising NaI(Tl), CsI(Tl) and CsI(Na) are more suitable for X-ray imaging.

Considering optical fiber as part of an imaging system, individual fibers can be bundled then tapered and coupled to a CCD detector. These tapered fibers have improved optics compared to a traditional lens due to less attenuation loss. The ability to attach optical fiber to these tapered optical fibers allows the potential to couple the light output from scintillating MOF to existing digital technology. Similarly, scintillating MOF is suited for directly attaching to the end of optical fiber for remote X-ray or gamma ray measurements.

The details of single crystal growth in MOF and similar optical waveguide structures is intended to aid future researchers by supplying details for the experimental technique and also describe what parts of the approach were successful and unsuccessful. The same considerations are extended to the material characterization of anthracene, which can apply to similar organic hydrocarbons. Future work in scintillating material is not limited to the organic and inorganic scintillator compounds. Improved scintillators, such as scintillating Quantum Dots and nanoparticles can also be incorporated into MOF.

This work presents the current state of the art fiber scintillator mechanism of TIR as the way to transmit scintillation light. This state of the art is extended to demonstrate a new and higher efficiency way light is transmitted in MOF with anthracene and alkali halide scintillators. This higher efficiency mechanism was found through repeated experimental observations. Additionally, this work has extended the scientific data for anthracene and alkali halide growth to show they can be grown in microstructured geometries over extended lengths. The anthracene fiber characterization provides additional scientific data anthracene. The theoretical work shows an approach to calculate fiber maximum light output when the TIR weakly guiding approximation is valid. These advances allow extending the scintillating fiber state of the art by incorporating scintillating materials in MOF.

REFERENCES

1. F.L. Pilar, *Chemistry the universal science*, Addison-Wesley Publishing, Reading, MA (1979).

2. G. F. Knoll, *Radiation Detection and Measurement*, publisher, John Wiley & Sons (2000), Ch 1, 8 & 14.

3. J.D. Jannopoulos, R.D. Meade, and J.N. Winn, *Photonic crystals: molding the flow of light*, Princeton University Press, Princeton, NJ (1995).

4. J.R Sparks, et al. "Selective semiconductor filling of microstructured optical fiber. *J. Lightware Technol.* **21**, 2005–2008 (2011).

5. P. Jorge, et al. "Optical fiber sensing using quantum dots". *Sensors* **7**, 3489–3534 (2007).

6. B. Larrion, et al. "Photonic crystal fiber temperature sensor based on quantum dot nanocoatings". *J. Sens.* **7**, 797436:1–797436:6 (2009).

7. M. Pisco, et al. "Hollow fibers integrated with single wall carbon nanotubes: Bandgap modification and chemical sensing" *Sens. Actuators B* **129**, 163–170 (2008).

8. G.E. Town, W. Yuan, R. McCosker, O. Bang "Microstructured optical fiber refractive index sensor" *Opt. Lett.* **35**, 856–858 (2010).

9. R.E. Galian, M. Laferriere, J.C. Scaiano, "Doping of photonic crystal fibers with fluorescent probes: Possible functional materials for optrode sensors" *J. Mater. Chem.* **16**, 1679–1701 (2006).

10. J. Wang and T. Wang, "Liquid filled microstructured polymer fibers as monolithic liquid-core array fibers", Appl. Opt., **48**, 881-885 (2009).

11. T. Nasilowski, et al., "Sensing with photonic crystal fibers", Intelligent Signal Processing, WISP 2007 IEEE International Symposium on, 1-6, (Oct. 2007).

12. G. Vienne, et al., "Liquid core fibers based on hollow core microstructured fibers", Lasers and Electro-Optics, 2005. CLEO/Pacific Rim 2005. Pacific Rim Conference on, 551-555, (Aug. 2005).

13. F.M. Fox, A. Argyos, M.C.J. Large, "Liquid-filled hollow core microstructured polymer optical fiber", Opt. Exp., 14, 4135-4140, (2006).

14. M. Lelek, F. Louradour, V. Couderc, P. Viale, S. Fevrier, J. L. Auguste, J. M. Blondy, A. Barthelemy, "High sensitivity autocorrelator based on a fluorescent liquid core", Appl. Phys. Lett., 89, 061117(1-3) (2006).

15. J.C. Knight, J. Broeng, T.A. Birks, and P.S.J. Russell, "Photonic band gap guidance in optical fibers", Science 282, 1476-1478 (1998).

16. Y. Fink, D.J. Ripin, S. Fan, C. Chen, J.D. Jannopoulous, and E. L. Thomas, "Guiding optical light in air using an all-dielectric structure", J. Lightwave Tech. 17, 2039-2041 (1999).

17. J.C. Knight, "Photonic crystal fibres", Nature 424, 847-851 (2003).

18. J.B. Birks, *Theory and Practice of Scintillation Counting*, Paragon Press, NY, NY (1964).

19. P.A. Rodnyi, *Physical Processes in Inorganic Scintillators* CRC Press, NY, NY, (1997).

20. H. Leutz, "Scintillating Fibers", Nucl. Instr. and Meth. 364, 442–448 (1995).

21. L. Hammar, "Novel design of high resolution imaging x-ray detectors" in *18thWorld Conference on Nondestructive Testing*, April 16-20, Druban, South Africa (2012).

22. S.L. DeHaven, S. Albin, and W. Kelliher, "Liquid filled microstructured optical fiber for X-ray detection" Opt. Express **18**, 13754-13760 (2010).

23. S.L. DeHaven, R.A. Wincheski, and S. Albin, "Anthracene Fibers Grown in a Microstructured Optical Fiber for X-ray Detection", Materials **7(9)**, 6291-6303 (2014).

24. S.L. DeHaven, R.A. Wincheski, and S. Albin, "Alkali Halide Microstructured Optical Fiber for X-ray Detection" Rev. Prog. QNDE 41 AIP Conf. Proc. Submitted for publication (2014).

25. S.L. DeHaven, "Microstructured optical fiber for x-ray detection" Rev. Prog. QNDE 29 AIP Conf. Proc. **1121** 541-548 (2009).

26. FIMMWAVE from Photon Design: http://www.photond.com.

27. CUDOS Multipole Analysis Software for Microstructured Fiber: http://sydney.edu.au/science/physics/cudos/research/mofsoftware.shtml

28. D. Gloge "Weakly Guiding Fibers", Appl. Opt.., **10**, 2252-2258 (1971).

29. A.W Snyder and J.D. Love, *Optical Waveguide Theory*, Chapman and Hall, NY, NY (1983), Chap. 1-6.

30. J. J. Fitzgerald, G.L. Brownell, G.L., F.J. Mahoney, F.J., *Mathematical Theory of Radiation Dosimetry*, Gordon and Breach Science, NY, NY (1967), Chap. 5.

31. K.A. Jackson, D.R. Ulmann, and J.D. Hunt,"On the nature of crystal growth from the melt", J. Cryst. Growth1, 1-36 (1967).

32. R. A. Laudise, *The growth of single crystals*, Prentice-Hall, Englewood Cliffs, NJ, 1970, Chaps 2, 3,5.

33. D. P. Woodruff, *The solid-liquid interface*, Cambridge University Press, New York, 1973, Chap. 3.

34. G.E. Ham, "The role of symmetry in crystallization and polymerization phenomena", J. Poly. Sci. **61**, 293-302 (1962).

35. A.S. Dworkin and M.A. Bredig, "The heat of fusion of the alkali metal halides" J. Phys. Chem. **64(2)**, 269-272 (1960).

36. H. Biederman, S.M. Ojha, L. Holland "The properties of fluorocarbon films prepared by R.F. sputtering and plasma polymerization in inert and active gas" Thin Solid Films **41**, 329–339 (1977).

37. Saint Gobian Liquid Scintillator Products: http://www.detectors.saint-gobain.com/Liquid-Scintillator.aspx.

38. J.B. Birks "The fluorescence and scintillation decay times of crystalline anthracene" Proc. Phys. Soc. **79**, 494–496 (1962).

39. M. Sano, M. Pope, and H. Kallmann, "Electroluminescence and band gap in anthracene", J. Chem. Phys. **43**, 2920-2921, (1964).

40. F.H. Babai and E,A,D White "The growth of void-free crystal cored fibres of organic materials", J. Cryst. Growth, **49**, 245-252 (1980).

41. N. Uenishi, et. al. Sumitomo Electric Industries, "Method for producing organic crystal and crystal growth therefor", U.S. Pat. 5363797, Nov. 15 (1994).

42. A. Arulchakkaravarthi et. al. , "Investigations on the growth of anthracene and trans-stilbene single crystals using vertical Bridgman technique" Mat. Sci. and Engr. **B95** 236-241 (2002).

43. S. Wiederhorn, H.G. Drikamer, "The effect of pressure on the near-ultra-violet spectra of some fused-ring aromatic crystals", J. Phys.Chem. Solids **9**, 330–334 (1959).

44. J. Rasanen, F. Stenman, and E. Penttinen, "Raman scattering from molecular crystals – II. Anthracene" Spect. Acta **29A**, 395-403 (1973).

45. K.E. Sterin, V.T. Aleksanyan, and G.N. Zhizhin, *Raman Spectra of Hydrocarbons* Pergamon Press, NY, NY (1980) pp 326.

46. N. Abasbegovic, N. Vukotic, and L. Colombo, "Raman Spectrum of Anthracene" J. Chem. Phys. **41**, 2575-2577 (1964).

47. M. Suzuki, T. Yokoyama, and M. Ito, "Polarized Raman spectra of naphthalene and anthracene single crystals" Spect. Acta. **24**, 1091-1107 (1968).

48. J.R Ferraro and K. Nakamoto, *Introductory Raman Spectroscopy*, Academic Press, NY, NY (1994) Chap.1 & 2.

49. J.C. Vickerman, *Surface Analysis*, John Wiley & Sons, NY, NY (1997).

50. ICDD Anthracene PDF # 00-039-1848 (1988).

51. S. Jo, H.Yoshikawa, A. Fujii, M. Takegana, "Surface morphologies of anthracene single crystals grown from vapor phase" Appl. Surf. Sci. **252**, 3514–3519 (2006).

52. H. Li, D. Zhang, L. Duan, G. Dong, L. Wang, Y. Qiu, "Morphological structure and optical property of anthracene single crystal grown from solution" Jpn. J. Appl. Phys. **46**, 7789–7792 (2007).

53. G. Madhurambal, P.A. Srinivasan, "Growth of high quality anthracene crystals by a simple solution technique" Cryst. Res. Technol. **41**, 231–235 (2006).

54. ICDD Sodium Fluoride PDF # 00-036-1455 (1986).

55. B.D. Cullity *Elements of X-ray Diffraction*; Addison-Wesley: Reading, MA (1978) pp. 32–80.

56. V. Ern, R.E. Merrifield "Magnetic field effect on triplet exciton quenching in organic crystals" Phys. Rev. Lett. **21**, 609–611 (1968).

57. R. Belaid, T. Barhoumi, L. Hachani, L. Hassine, H. Bouchriha, "Magnetic field effect on recombination light in anthracene crystal".. Synth. Met. **131**, 23–30 (2002).

58. Z.G. Soos, "Zeeman populations of optically produced triplet excitons in anthracene" J. Chem. Phys. **51**, 2107–2112 (1969).

59. S. Wiederhorn, H.G. Drikamer, "The effect of pressure on the near-ultra-violet spectra of some fused-ring aromatic crystals" J. Phys.Chem. Solids **9**, 330–334 (1959).

60. K. Hummer, P. Puschnig, C. Ambroschdraxl, M. Oehzelt, G. Heimel, R. Resel, "Calculated optical absorption of anthracene under high pressure" Synth. Met. **137**, 935–936 (2003).

VITA

Stanton DeHaven
752 E Little Back River Rd
Hampton, VA 23669

Received his BSME and MSME degrees in 1984 and 1987, respectively from the

University of Kentucky. Received the MEEE degree from Old Dominion University in

2001. Performed systems engineering work at Newport News Shipbuilding from 1988-

1991. Performed process systems engineering at NASA Langley from 1991-2002 on

wind tunnels. Attained the professional engineer's license in 1998. Performed fiber

optics sensors research and development from 2002-2014. Has published six conference

papers and three journal papers and has one patent pending. His research interests

include sensor technologies for nondestructive testing.

Selected publications:

1. S.L. DeHaven, R.A. Wincheski, and S. Albin, "Alkali Halide Microstructured Optical Fiber for X-ray Detection" Review of Progress in Quantitative Nondestructive Evaluation, Vol. 34, edited by D. E. Chimenti and L. J. Bond, published by AIP, Melville, NY (2015).

2. S.L. DeHaven, R.A. Wincheski, and S. Albin, "Anthracene Fibers Grown in a Microstructured Optical Fiber for X-ray Detection", Materials 7(9), 6291-6303 (2014).

3. S.L. DeHaven, S. Albin, W. Kelliher,"Liquid filled microstructured optical fiber for x-ray detection", Opt. Express V18 13754-13760 (2010).

4. S.L. DeHaven "Microstructured optical fiber for x-ray detection" Rev. Prog. QNDE 29 AIP Conf. Proc. Vol. 1211, 541-548 (2009).